Synthetic Siglec-9 agonists inhibit neutrophil activation associated with COVID-19

Authors.

Corleone S. Delaveris,[1,2] Aaron J. Wilk,[3,4,5] Nicholas M. Riley,[1] Jessica C. Stark,[1] Samuel S. Yang,[6] Angela J. Rogers,[5] Thanmayi Ranganath,[5] Kari C. Nadeau,[5,7] the Stanford COVID-19 Biobank,[8] Catherine A. Blish,[5,9] Carolyn R. Bertozzi[1,2,10]

Author Affiliations.

[1]Department of Chemistry, Stanford University, Stanford CA, 94305

[2]ChEM-H, Stanford University, Stanford, CA 94305

[3]Stanford Medical Scientist Training Program, Stanford, CA 94305

[4]Stanford Immunology Program, Stanford University, Stanford, CA 94305

[5]Department of Medicine, Stanford University, Stanford, CA 94305

[6]Department of Emergency Medicine, Stanford University, Stanford, CA 94305

[7]Sean N. Parker Center for Allergy and Asthma Research, Stanford, CA, 94305

[8]Stanford Biobank, Stanford University, Stanford, CA 94305

[9]Chan Zuckerberg Biohub, San Francisco, CA 94158

[10]Howard Hughes Medical Institute, Stanford, CA 94305

Abstract.

Severe cases of coronavirus disease 2019 (COVID-19), caused by infection with SARS-CoV-2, are characterized by a hyperinflammatory immune response that leads to numerous complications. Production of proinflammatory neutrophil extracellular traps (NETs) has been suggested to be a key factor in inducing a hyperinflammatory signaling cascade, allegedly causing both pulmonary tissue damage and peripheral inflammation. Accordingly, therapeutic blockage of neutrophil activation and NETosis, the cell death pathway accompanying NET

formation, could limit respiratory damage and death from severe COVID-19. Here, we demonstrate that synthetic glycopolymers that activate signaling of the neutrophil checkpoint receptor Siglec-9 suppress NETosis induced by agonists of viral toll-like receptors (TLRs) and plasma from patients with severe COVID-19. Thus, Siglec-9 agonism is a promising therapeutic strategy to curb neutrophilic hyperinflammation in COVID-19.

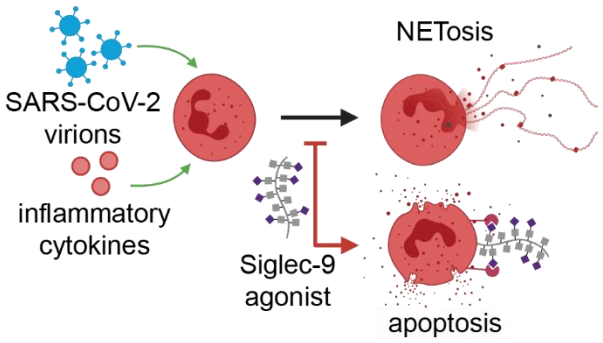

Abstract Figure. In COVID-19, viral pathogen associated molecular patterns and viral-induced cytokines can induce NETosis of neutrophils at the site of infection and in the periphery. Siglec-9 agonists inhibit COVID-19 plasma-induced NETosis, potentially preventing deleterious hyperinflammatory responses.

Introduction.

Runaway inflammation in coronavirus disease 2019 (COVID-19) is thought to lead to numerous complications, including potentially fatal pneumonia and acute respiratory distress syndrome (ARDS).[1–3] While the specific causal factors of inflammation in COVID-19-related ARDS are unknown and likely multifarious, an emerging hypothesis posits that hyperactivation of neutrophils initiates and drives this response (**Figure 1**).[4–12] Neutrophils are immune cells of the myeloid lineage that are involved in numerous innate immune functions. It has been suggested that neutrophils drive a hyperinflammatory response in COVID-19 through a death process called NETosis, in which neutrophils rapidly decondense chromatin and spew out a neutrophil extracellular trap (NET), an amalgam of genomic DNA, intracellular proteins (e.g. histones), and tissue-damaging enzymes (e.g. neutrophil elastase, myeloperoxidase).[13,14] Extracellular DNA and tissue damage from NET-associated enzymes act as proinflammatory signals to other immune cells [15–17] and are proposed to initiate the hyperinflammatory cascade in COVID-19, leading to ARDS and potentially death. Consistent with this hypothesis, NETs have been extensively observed both at the site of infection (i.e., pulmonary tissue) [18–21] and in the periphery (i.e., sera and plasma).[19,21]

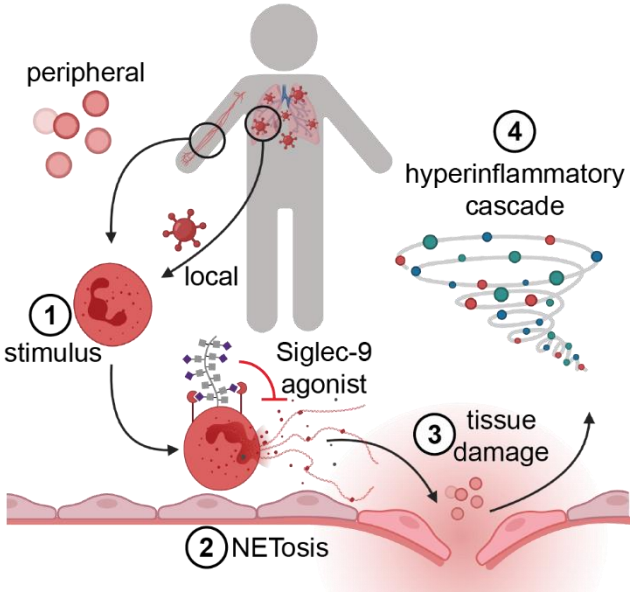

Figure 1. Local and peripheral inflammatory stimuli induce NETosis and a subsequent hyperinflammatory cascade in COVID-19. Both local inflammatory stimuli at the site of SARS-CoV-2 infection (e.g. virions) and peripheral inflammatory stimuli (e.g. the proinflammatory cytokines IL-8 and G-CSF) associated with COVID-19 have been shown to induce NETosis *in vitro*. These factors are suspected to be causative agents of NETosis in those tissues, initiating a deleterious hyperinflammatory cascade leading to the symptoms of moderate and severe COVID-19. Agonists of the neutrophil-associated checkpoint receptor Siglec-9 could inhibit NETosis in COVID-19.

Both SARS-CoV-2 virions and serum/plasma from COVID-19 patients have been shown to induce NETosis of neutrophils isolated from healthy donors *in vitro*, consistent with both the local and peripheral inflammatory responses observed in COVID-19.[19,21,22] However, the specific signals that induce NETosis in viral disease remain an open question; viral ligands for toll-like receptors (TLRs), host damage-associated molecular patterns, antiviral cytokines (e.g., IL-8 and IFNγ), and activated platelets have all been implicated, but which if any of these is sufficient to induce NETosis is still debated.[21,23] Beyond viral disease, NETosis has been demonstrably

linked to numerous inflammatory pathologies, including thrombosis and sepsis, both of which are observed in patients with COVID-19.[4] During NETosis, inflammatory stimuli signal neutrophils to import calcium ions, which activates protein arginine deiminase 4 (PADI4).[24,25] PADI4 mediates the conversion of arginine to the deiminated citrulline on histones.[25] The loss of positive charges induces rapid unwinding of genomic DNA, which eventually ruptures the nucleus and the cell.[25] When this happens, intracellular contents including genomic DNA, active PADI4, tissue-damaging NET-associated enzymes, and citrullinated histones are emitted into the extracellular space, all of which provoke an inflammatory response.[24,25] Thus, strategies to curb neutrophil-mediated inflammation could treat both COVID-19 as well as other neutrophilic inflammatory pathologies.

Transcriptomic analyses of immune cells from severe COVID-19 patients show that neutrophils upregulate the myeloid checkpoint receptor Siglec-9, a member of the sialic acid-binding immunoglobulin-like lectin (Siglec) family that is also found on macrophages and activated T cells.[8,9,26–29] This sialoglycan-binding immunosuppressive receptor has an intracellular signaling domain similar to the prominent lymphoid checkpoint molecule PD-1.[30,31] And analogous to PD-1, clustering of Siglec-9 by virtue of ligand engagement leads to inhibitory signaling that quenches activation of the immune cells. Both erythrocytes and host-mimicking pathogens have been shown to engage Siglec-9 to suppress neutrophil-mediated immunity.[32–35] Furthermore, engagement of Siglec-9 on primary neutrophils has been shown to induce apoptotic pathways,[26] in a manner similar to the engagement of Siglec-8 on eosinophils that recently led to an FDA-approved Siglec-8 agonist for eosinophilic inflammatory conditions.[36] Given that Siglec-9 is both anti-inflammatory and pro-apoptotic checkpoint molecule, we hypothesized that engagement of Siglec-9 could simultaneously inhibit proinflammatory NETotic cell death and induce quiet apoptotic cell death in COVID-19-related inflammation. Notably, an agonist (CD24Fc, tradename SACCOVID) of the related myeloid checkpoint receptor Siglec-10

has recently shown great promise in suppressing viral hyperinflammation and is in a Phase III clinical trial.[37,38] However, unlike the CD24/Siglec-10,[39] a specific and high-affinity glycoprotein ligand for Siglec-9 has not been described.[40]

We recently reported[41] the design and synthesis of a potent Siglec-9 agonist comprising a lipid-conjugated glycopolypeptide bearing modified sialic acid residues that Paulson and coworkers had previously found to confer high-affinity and specificity binding to Siglec-9 over other Siglec family members (pS9L, **Figure 2**).[42] The lipid group enabled passive insertion into cell membranes, leading to engagement of Siglec-9 in cis on macrophage cell surfaces. This cell-surface clustering, in turn, induced Siglec-9 signaling suppress macrophage activation.[41] In this recent study we also designed control glycopolypeptides lacking either Siglec-9 binding glycans (i.e., the lactose-functionalized glycopolypeptide pLac) or a membrane anchoring lipid group (i.e., the soluble glycopolypeptide pS9) (**Figure 2**). Notably, potent Siglec-9 agonism required membrane anchoring and cis-engagement; the soluble congener pS9 was inable to stimulate Siglec-9 signaling and suppress macrophage activity. We hypothesized that pSL9 might also be able to suppress neutrophil activation and NETosis by clustering Siglec-9 on neutrophils.

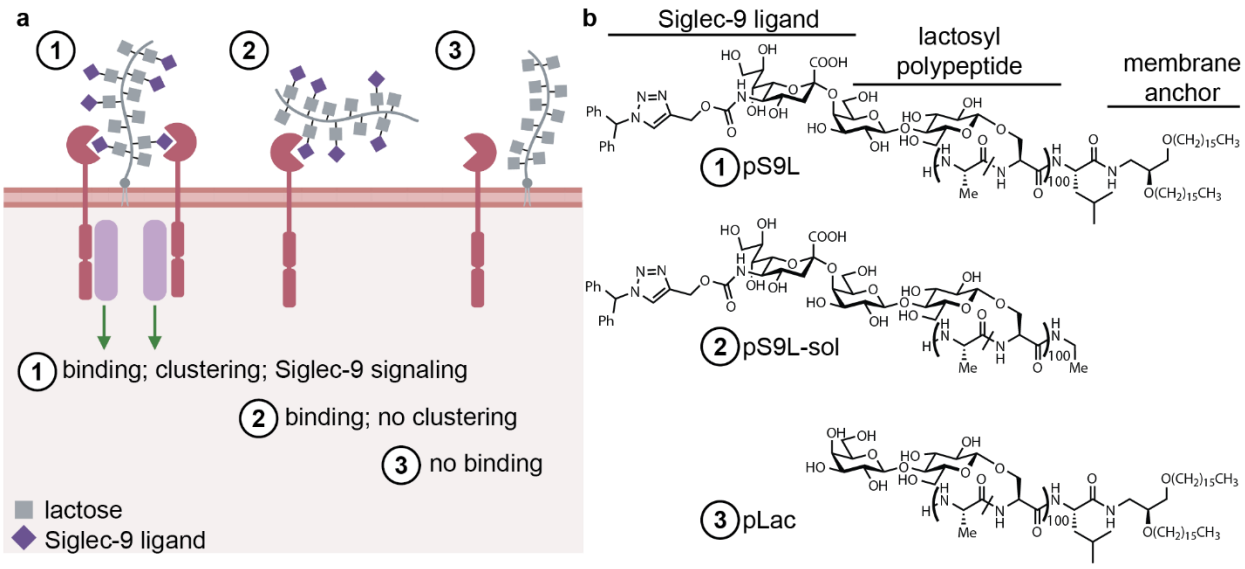

Figure 2. Synthetic glycopolypeptides bearing high-affinity Siglec-9 ligands cluster and engage Siglec-9 signaling. (**a**) Membrane-anchored and cis binding glycopolypeptide **1** (pS9L) induces Siglec-9 signaling, while a non-cis binding control polypeptide **2** (pS9L-sol) or a non-binding but membrane-anchored control polypeptide **3** (pLac) do not. (b) Structures of the polypeptides **pS9L**, **pS9L-sol**, and **pLac**. Polypeptides are all based on an *O*-lactosyl poly-serine-co-alanine scaffold, and in some cases bear terminal Siglec-9 ligands and/or C-terminal membrane-anchoring lipids.

Here, we demonstrate that a synthetic cis-binding Siglec-9 agonist (pS9L, **Figure 2b**)[41] inhibits NETosis in primary neutrophils in models of local (TLR-7/8 agonist) and peripheral (COVID-19 plasma) COVID-19-associated inflammation. Using time-course live cell microscopy, we showed that TLR-7/8 activation by the nucleoside analog resimiquod (R848) is sufficient to induce specific NETosis in primary human neutrophils. R848 induces rapid citrullination of histone substrates, consistent with PADI4-mediated NETosis, and this process was blocked by Siglec-9 signaling induced by pS9L. SIgnificantly, pS9L inhibited neutrophil NETosis induced by

treatment with plasma from severe COVID-19 patients. In light of these data, we propose that Siglec-9 agonists could be therapeutic agents that inhibit COVID-19-associated inflammation.

Results and Discussion.

TLR-7/8 agonist R848 induces NETosis of primary neutrophils *in vitro*.

In COVID-19, evidence of extensive NETosis can be observed in infected lungs,[18–21] and SARS-CoV-2 virions have been shown to infect and induce NETosis of healthy neutrophils *in vitro*.[20] These reports implicate TLR-7 and/or TLR-8 in inducing NETosis of neutrophils at the site of infection.[20,43] Notably, TLR-7 and TLR-8 are ssRNA receptors with numerous substrates identified in the SARS-CoV-2 genome.[44] Furthermore, consistent with the hypothesis that SARS-CoV-2 induces TLR-7/8-mediated immunity, TLR-7 deficiency is associated with severe COVID-19.[45] Thus, agonists of TLR-7/8 may provide a convenient means of modeling local inflammation induced by viral infection *in vitro* without using live virus.

We assayed TLR agonists using the live-cell imaging techniques described by Gupta and coworkers.[46] In this assay, freshly isolated neutrophils are cultured in low-serum media in the presence of a fluorogenic and membrane impermeable DNA-intercalating dye (Cytotox Green). Upon genomic DNA-externalization by NETosis, dye intercalates and fluorescence increases. As previously demonstrated,[46] because NETs are much larger than the nuclei of apoptotic cells, NETotic cells yield much larger areas of fluorescence than apoptotic cells, as observed by microscopy. Thus, apoptotic cells can be filtered out by only counting large (i.e., >>100 μm^2) fluorescent objects.

We found that a TLR-7/8 agonist, R848, was sufficient to induce NETosis of healthy neutrophils *in vitro* (**Figure 3a-c, Figure S1**). We also assayed the citrullination status of the PADI4 substrate H3 by Western blot, and observed that R848 rapidly induced citrullination at R2, R8,

and R17 (**Figure S2**). Additionally, we performed quantitative phosphoproteomics[47] with lysates of neutrophils treated with media, phorbol-12-myristate-13-acetate (PMA), or R848 (**Figure S3**, **Table S1**). We observed similar results to previously published datasets using neutrophils stimulated with either R848[48] or PMA[49]. Furthermore, several phosphosites were found to be differentially regulated in both datasets, including those involved in neutrophil degranulation and calcium flux, consistent with the described mechanism of NETotic death.[24,49] These results indicate that the TLR-7/8 agonist R848 induces NETosis in primary neutrophils. Thus, this can be used to model local inflammation associated with viral infection, including in COVID-19.

A Siglec-9 agonist inhibits TLR-7/8-induced NETosis via SHP-1.

Previous studies by von Guten and coworkers have shown that engagement of Siglec-9 leads to apoptotic and nonapoptotic death pathways as well as immunosuppression in neutrophils.[26,32] Thus, we hypothesized that Siglec-9 mediated immunosuppression and cell death could override the NETotic effect of antiviral TLR signaling. To assay this, we employed the synthetic Siglec-9 cis-binding agonist, pS9L, that we have previously described.[41] pS9L is a lipid-tethered glycopolypeptide, biomimetically inspired by native mucin proteins (**Figure 2**). When the lipid inserts into the cell membrane, the polypeptide backbone can adopt extended conformations,[50] resulting in presentation of multivalent high-affinity Siglec-9 cis ligands.[41] We have previously observed that presentation in this manner results in binding and clustering with Siglec-9 in cis.[41] We additionally used two control glycopolypeptides: pLac, a lipid-tethered glycopolypeptide based on the same scaffold as pS9L, but lacking terminal Siglec-9 binding sialosides, and pS9L-sol, a soluble lipid-free analogue of pS9L incapable of binding in cis (**Figure 2, S4**).

We assayed anti-NETotic activity by cotreatment of glycopolypeptide (500 nM) with R848 (10 μM) in primary neutrophils in the live-cell assay described above (**Figure 3**). We observed that pS9L was sufficient to inhibit NETosis induced by R848 treatment (**Figure 3a-c**). Moreover,

neither control polymer inhibited R848-induced NETosis (**Figure 3d**). We also confirmed that pS9L inhibits NETosis comparably to high concentrations of crosslinked anti-Siglec-9 antibody (clone 191240) (**Figure S5**). [51,52] Additionally, we found that treatment with pS9L induced an oxidative burst in primary neutrophils (**Figure S6**), which von Guten and coworkers described as an important signaling step of Siglec-9-induced apoptotic signaling.[26] Furthermore, the oxidative burst was inhibited by the addition of the SHP-1/2 inhibitor NSC-87877, suggesting that SHP-1 and/or SHP-2 mediate pS9L-induced oxidative burst in neutrophils, consistent with Siglec-9 engagement (**Figure S6b**).

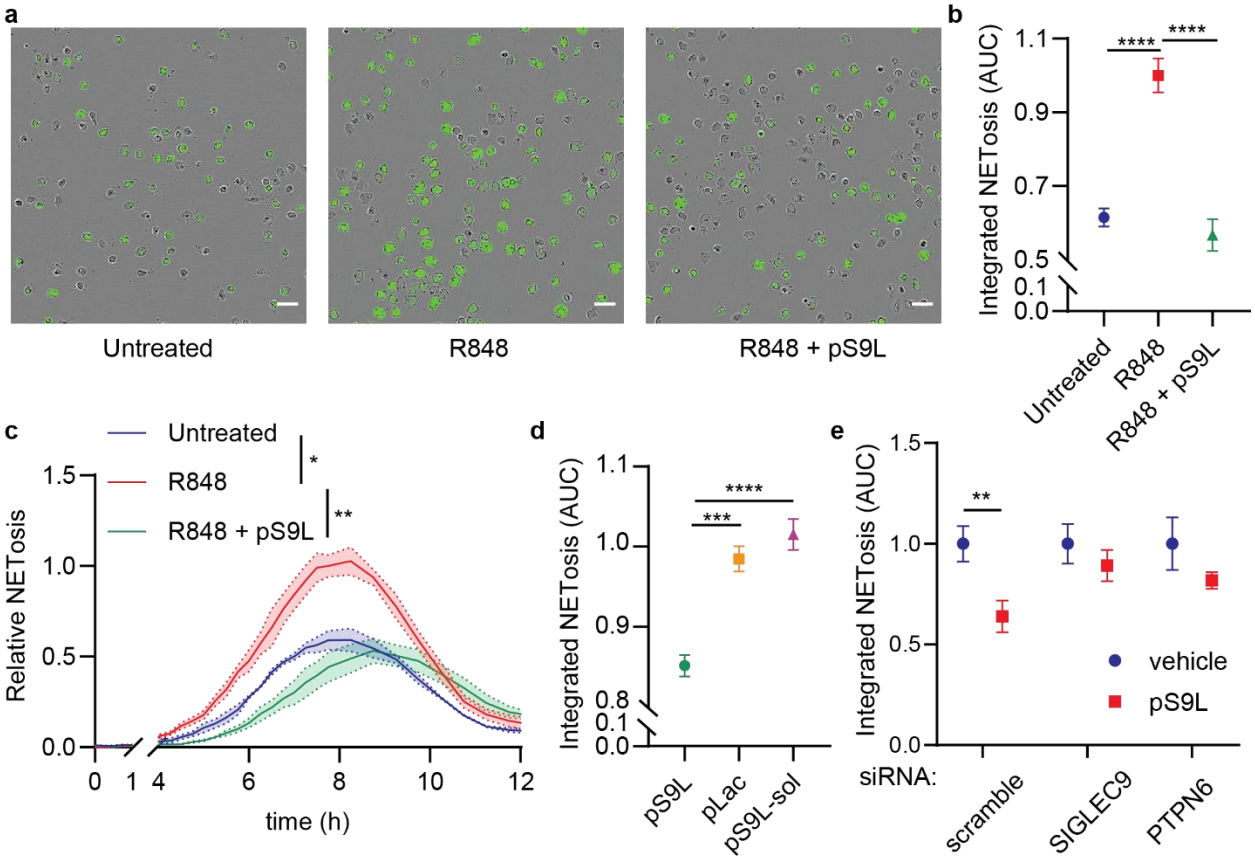

Figure 3. A cis-binding Siglec-9 agonist (pS9L) inhibits R848-induced NETosis via Siglec-9 and SHP-1. (**a**-**c**) Primary neutrophils were cotreated with R848 (10 μM) and glycopolypeptide (500 nM) in IMDM supplemented 0.5% hiFBS containing the membrane impermeable DNA intercalators Cytotox Green or Red (250 nM). Images were acquired by fluorescence

microscopy every 15 min for 12 h. The area of all green fluorescent objects >300 μm^2 was quantified and the total area was averaged across three images per well. Relative NETosis was determined by normalizing to the maximal NET area from R848 treatment alone (t = 8 h). (**a**) Representative phase contrast and fluorescence images from t = 8 h. Scale bars indicate 40 µm. (**b**) Quantitation of NETosis over time as area under the curve in (**c**). Error bars represent SD. (**c**) NET formation and degradation as a function of time. Error bands represent SEM. (**d**) Treatment of R848-stimulated neutrophils with various glycopolypeptides. Error bars represent SD. (**e**) pS9L is a mucin-like glycopolypeptide that bears high affinity and specific ligands for Siglec-9 and is functionalized with a membrane-tethering lipid tail. (**f**) HL-60 cells were transfected with siRNAs against SIGLEC9 (encoding Siglec-9), PTPN6 (encoding SHP-1), or a scrambled control and then grown for two days. Cells were then cotreated with R848 (10 µM) and vehicle or pS9L (500 nM). Relative NETosis is determined as in (**b**), except all objects >200 μm^2 were quantified and the R848 maximum in dHL-60's was observed at 2.5 h post induction. Error bars represent SD. Statistics were determined by two-way ANOVA (**b**) or one-way ANOVA (**c**,**d**,**f**). * $p < 0.05$; ** $p < 0.01$; *** $p < 0.001$; **** $p < 0.0001$.

We performed quantitative phosphoproteomics using lysates of R848-stimulated primary neutrophils cotreated with vehicle, pS9L, or pLac (**Figure S3**, **Table S2**). Notably, we found increased phosphorylation of hyccin (HYCCI / FAM126A), a key component in phosphorylation of phosphoinositides,[53] a class of signaling molecules implicated in mediating NETosis.[54] Additionally, we observed increased phosphorylation of RASAL3 (RASL3), a negative regulator of the MAPK signaling pathway.[55] These data suggest that pS9L inhibits the calcium flux and NADPH activity necessary for NETosis, as well as the MAPK-suppressive effects that have been previously described for pS9L in macrophages.[41]

To determine whether the anti-NETotic effect of pS9L is specifically mediated by Siglec-9 signaling, we recapitulated our results in the HL-60 cell line. The HL-60 line is a promyelocytic leukemia that can be differentiated into a neutrophil-like cells (dHL-60) using all-trans retinoic acid (ATRA, 100 nM) and dimethylsulfoxide (DMSO, 1.25% v/v), which have previously been used to study NETosis *in vitro*.[31,56] We observed that R848 induced NETosis in dHL-60 cell's (**Figure S7**). Furthermore, we observed that pS9L inhibited NETosis and that siRNA knockdown of Siglec-9 (encoded by *SIGLEC9*) or SHP-1 (encoded by *PTPN6*) abrogated the effect of pS9L (**Figure 3e**, **S8**, **S9**). Therefore, the Siglec-9 agonist pS9L inhibits TLR7/8-induced NETosis via Siglec-9 and SHP-1. This suggests that Siglec-9 agonists could inhibit NETosis at the site of viral infection, thus preventing pulmonary inflammation in COVID-19.

Siglec-9 is upregulated in severe COVID-19 and can inhibit NETosis induced by COVID-19 plasma.

Sera and plasma from COVID-19 patients have been shown to be sufficient to induce NETosis of neutrophils isolated from healthy donors *in vitro*.[19,21] The causes of this are unclear, however potential factors include viral TLR ligands, damage-associated molecular patterns that bind TLRs, activated platelets, and (pro)inflammatory cytokines. Recent reports have described increased levels of neutrophil-activating cytokines, predominantly IL-8 and G-CSF.[57] Consistent with this observation, we also observed that the combination of IL-8 and G-CSF was sufficient to induce NETosis *in vitro* (**Figure S10**). Additionally, transcriptomic analyses of peripheral myeloid cells[8] and neutrophils[9] in COVID-19 patients have observed increased *SIGLEC9* expression (**Figure 4a, S11**) and *PADI4* expression (**Figure 4b**, **S11**). We hypothesize that this is an exhaustion-like phenotype of induced Siglec-9 expression of hyper-NETotic neutrophils, similar to what has been observed with Siglec-9 on exhausted tumor-infiltrating T cells.[51] This makes Siglec-9 an attractive target for therapeutic blockade of hyperinflammatory NETosis in COVID-19.

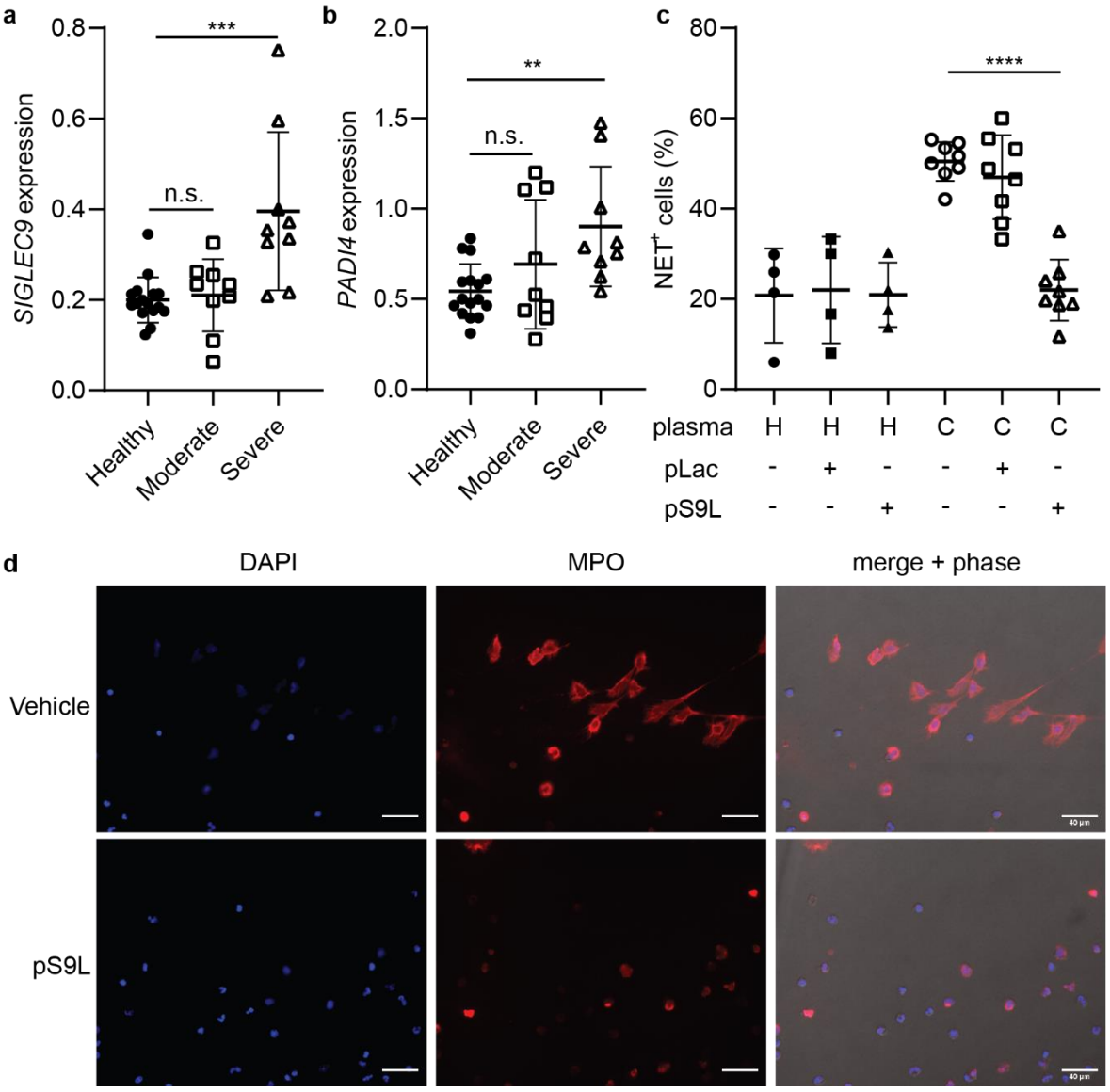

Figure 4. A Siglec-9 agonist inhibits NETosis of neutrophils induced by COVID-19 plasma. (**a**,**b**) Analysis of publicly available single-cell transcriptomics data [8] for *SIGLEC9* expression (**a**) and *PADI4* expression (**b**) on neutrophils in peripheral blood from healthy donors or COVID-19 patients. Error bars represent SD. Statistics were determined using mixed effects model. ** = $p < 0.01$; *** = $p < 0.001$ (**c,d**) Primary neutrophils were cultured in undiluted and citrate anticoagulated plasma from healthy donors or COVID-19 patients for 4 h. Cells were fixed, stained for extracellular myeloperoxidase, and imaged in DAPI imaging media by fluorescence microscopy. Cells were treated in technical triplicate and imaged across multiple fields of view.

(**c**) Proportion of NET-positive cells (%) across all fields of view. Each dot represents and individual plasma sample. (**d**) Representative images from a COVID-19 patient plasma sample with or without pS9L. Error bars represent SD. Statistics were determined using mixed effects models to account for samples using repeat neutrophil donors. **** = $p < 0.0001$.

To test the hypothesis that pS9L can inhibit NETosis induced by COVID-19 plasma, we treated neutrophils isolated from whole blood of healthy donors with citrate-anticoagulated heterologous plasma from healthy donors or COVID-19 patients. Neutrophils in undiluted plasma were cotreated with pS9L (500 nM), the non-binding analog pLac (500 nM), or vehicle. To satisfy biosafety restrictions, cells were incubated in the presence of COVID-19 plasma for 4 h and then fixed before assaying for extracellular complexes of myeloperoxidase (MPO) and DNA (DAPI) (**Figure 4c**,**d**). The combination of these stains, which when observed extracellularly is indicative of NETosis, has been previously used to identified NET^+ cells in the context of COVID-19.[20] We observed that COVID-19 plasma induced NETosis of neutrophils from healthy donors, and that this effect was inhibited by pS9L (**Figure 4c**,**d**). This is indicated by the distinct web-like morphology of NETs (**Figure 4d**). Furthermore, we observe that pLac does not inhibit COVID-19-induced NETosis, and that neither polymer effects basal NETosis of *in vitro* cultured neutrophils (**Figure 4c**). Additionally, we performed similar experiments staining neutrophils treated with 10% plasma in IMDM (**Figure S12**) or undiluted plasma (**Figure S13**) for extracellular H1/DNA complexes, another marker of NETs,[58–60] and observed comparable results.

Collectively, these data demonstrate that Siglec-9 agonists are sufficient to inhibit NETosis induced by COVID-19 patient plasma, and thus could inhibit peripheral inflammation in patients with COVID-19. Additionally, Siglec-9 agonists could resolve NET-associated pathologies observed in COVID-19 and elsewhere such as immunothrombosis[21] and sepsis.[4,5]

Conclusion.

Here, we have demonstrated that Siglec-9 agonists can inhibit NETosis induced by COVID-19-associated proinflammatory signals. Thus, if NETosis is a causal factor of COVID-19-related hyperinflammation as has been hypothesized, Siglec-9 is a therapeutic target to inhibit potentially fatal hyperinflammation associated with COVID-19 in an analogous fashion to the highly effective therapeutics currently aimed at the Siglec-10/CD24 interaction. A CD24-Fc fusion protein has been shown to both engage Siglec-10 as an immune checkpoint on macrophages and sequester the nuclear protein HMGB1, which can act as a damage associated molecular pattern by engaging TLR4.[39] The Siglec-9 agonists described here have previously been shown to inhibit macrophage TLR4 signaling and engage macrophage Siglec-9.[41] Thus, Siglec-9 agonists may be multipurpose therapeutics, able to both inhibit the clinically unaddressed problem of proinflammatory NETosis and also subsequent inflammatory signaling from tissue damage that is currently being clinically investigated. Finally, Siglec-9 agonists have the potential to expand beyond ARDS to other NET-related pathologies such as thrombosis,[61,62] atherosclerosis,[63] and cystic fibrosis.[64]

Acknowledgements.

The authors would like to thank the following individuals at the Stanford COVID-19 Biobank for enabling this work: Nancy Zhao, Rosemary Vergara, Julia McKechnie, Aaron Wilk, Lauren de la Parte, Kathleen Whittle Dantzler, Maureen Ty, Nimish Kathale, Arjun Rustagi, Giovanny Martinez-Colon, Geoff Ivison, Ruoxi Pi, Maddie Lee, Rachel Brewer, Taylor Hollis, Andrea Baird, Michele Ugur, Drina Bogusch, Georgie Nahass, Kazim Haider, Thanmayi Ranganath, Kim Quyen Thi Tran, Laura Simpson, Michal Tal, Iris Chang, Evan Do, Andrea Fernandes, Shu-Chen Lyu, Wenming Zhang, Monali Manohar, James Krempski, Jonasel Roque, Hena Naz DinRosen Mann, Anita Visweswaran, Elizabeth J. Zudock, Kathryn Jee, Komal Kumar, Jennifer A. Newberry, James V. Quinn, Donald Schreiber, and Andra L. Blomkalns. The authors would

additionally like to thank: Rishi Kulkarni and Susan Holmes for their advice on statistics; Gabby Tender for her assistance with fluorescence microscopy. This work was supported by a grant from the National Institutes of Health to C.R.B. (CA227942). C.S.D was supported by a National Science Foundation Graduate Research Fellowship (DGE-114747) and a ChEM-H affiliated Stanford Interdisciplinary Gradate Fellowship. N.M.R. was funded through an NIH Predoctoral to Postdoctoral Transition Award (Grant K00 CA212454-05). J.C.S. was supported by an NIH/NCI F32 postdoctoral fellowship (Grant 1F32CA250324-01). A.J.W. was supported by the Stanford Medical Scientist Training Program (T32 GM007365-44) and the Stanford Bio-X Interdisciplinary Graduate Fellowship. C.A.B. was supported by the Burroughs Wellcome Fund Investigators in the Pathogenesis of Infectious Diseases #1016687 and the Bill and Melinda Gates Foundation (OPP1113682). C.A.B. is the Tashia and John Morgridge Faculty Scholar in Pediatric Translational Medicine from the Stanford Maternal Child Healthy Research Institute and an Investigator of the Chan Zuckerberg Biohub. Figure illustrations were created using BioRender.com.

Conflicts of Interest.

C.S.D. and C.R.B. are coinventors on a patent application for cis-binding Siglec agonist glycopolymers as immune suppressants (USPTO63046140). C.R.B. is a co-founder and Scientific Advisory Board member of Lycia Therapeutics, Palleon Pharmaceuticals, Enable Bioscience, Redwood Biosciences (a subsidiary of Catalent), and InterVenn Bio, and a member of the Board of Directors of Eli Lily & Company. C.A.B. is a Scientific Advisory Board member of Catamaran Bio.

References.

(1) Cao, X. COVID-19: Immunopathology and Its Implications for Therapy. *Nat. Rev. Immunol.* **2020**, *2019*, 2019–2020. https://doi.org/10.1038/s41577-020-0308-3.

(2) Mason, R. J. Pathogenesis of COVID-19 from a Cell Biology Perspective. *Eur. Respir. J.* **2020**, *55* (4), 9–11. https://doi.org/10.1183/13993003.00607-2020.

(3) Tay, M. Z.; Poh, C. M.; Rénia, L.; MacAry, P. A.; Ng, L. F. P. The Trinity of COVID-19: Immunity, Inflammation and Intervention. *Nat. Rev. Immunol.* **2020**, *20* (6), 363–374. https://doi.org/10.1038/s41577-020-0311-8.

(4) Thierry, A. R.; Roch, B. NETs By-Products and Extracellular DNA May Play a Key Role in COVID-19 Pathogenesis : Incidence on Patient Monitoring and Therapy. **2020**, No. April, 1–21. https://doi.org/10.20944/preprints202004.0238.v1.

(5) Barnes, B. J.; Adrover, J. M.; Baxter-Stoltzfus, A.; Borczuk, A.; Cools-Lartigue, J.; Crawford, J. M.; Daßler-Plenker, J.; Guerci, P.; Huynh, C.; Knight, J. S.; et al. Targeting Potential Drivers of COVID-19: Neutrophil Extracellular Traps. *J. Exp. Med.* **2020**, *217* (6), 1–7. https://doi.org/10.1084/jem.20200652.

(6) Liu, J.; Liu, Y.; Xiang, P.; Pu, L.; Xiong, H.; Li, C.; Zhang, M.; Tan, J.; Xu, Y.; Song, R.; et al. Neutrophil-to-Lymphocyte Ratio Predicts Severe Illness Patients with 2019 Novel Coronavirus in the Early Stage. *medRxiv* **2020**, *807*, 2020.02.10.20021584. https://doi.org/10.1101/2020.02.10.20021584.

(7) Bendib, I.; De Chaisemartin, L.; Granger, V.; Schlemmer, F.; Maitre, B.; Hüe, S.; Surenaud, M.; Beldi-Ferchiou, A.; Carteaux, G.; Razazi, K.; et al. Neutrophil Extracellular Traps Are Elevated in Patients with Pneumonia-Related Acute Respiratory Distress Syndrome. *Anesthesiology* **2019**, *130* (4), 581–591. https://doi.org/10.1097/ALN.0000000000002619.

(8) Schulte-Schrepping, J.; Reusch, N.; Paclik, D.; Baßler, K.; Schlickeiser, S.; Zhang, B.; Krämer, B.; Krammer, T.; Brumhard, S.; Bonaguro, L.; et al. Severe COVID-19 Is Marked by a Dysregulated Myeloid Cell Compartment. *Cell* **2020**, 1–22. https://doi.org/10.1016/j.cell.2020.08.001.

(9) Aschenbrenner, A. C.; Mouktaroudi, M.; Krämer, B.; Antonakos, N. Neutrophil Transcriptomes Stratify COVID-19 Patients Signatures in Blood. *medRxiv* **2020**, 1–56.

(10) Wilk, A. J.; Rustagi, A.; Zhao, N. Q.; Roque, J.; Martínez-Colón, G. J.; McKechnie, J. L.; Ivison, G. T.; Ranganath, T.; Vergara, R.; Hollis, T.; et al. A Single-Cell Atlas of the Peripheral Immune Response in Patients with Severe COVID-19. *Nat. Med.* **2020**, *26* (7), 1070–1076. https://doi.org/10.1038/s41591-020-0944-y.

(11) Bost, P.; De Sanctis, F.; Canè, S.; Ugel, S.; Donadello, K.; Castellucci, M.-N.; Eyal, D.; Fiore, A.; Anselmi, C.; Barouni, R. M.; et al. Deciphering the State of Immune Silence in Fatal COVID-19 Patients. *medRxiv* **2020**, 2020.08.10.20170894.

(12) Overmyer, K. A.; Shishkova, E.; Miller, I. J.; Balnis, J.; Bernstein, M. N.; Peters-Clarke, T. M.; Meyer, J. G.; Quan, Q.; Muehlbauer, L. K.; Trujillo, E. A.; et al. Large-Scale Multi-Omic Analysis of COVID-19 Severity. *Cell Syst.* **2020**, 1–18. https://doi.org/10.1016/j.cels.2020.10.003.

(13) Remijsen, Q.; Kuijpers, T. W.; Wirawan, E.; Lippens, S.; Vandenabeele, P.; Vanden Berghe, T. Dying for a Cause: NETosis, Mechanisms behind an Antimicrobial Cell Death Modality. *Cell Death Differ.* **2011**, *18* (4), 581–588. https://doi.org/10.1038/cdd.2011.1.

(14) Brinkmann, V.; Reichard, U.; Goosmann, C.; Fauler, B.; Uhlemann, Y.; Weiss, D. S.; Weinrauch, Y.; Zychlinsky, A. Neutrophil Extracellular Traps Kill Bacteria. *Science (80-.).* **2004**, *303* (5663), 1532–1535. https://doi.org/10.1126/science.1092385.

(15) Daniel, C.; Leppkes, M.; Muñoz, L. E.; Schley, G.; Schett, G.; Herrmann, M. Extracellular DNA Traps in Inflammation, Injury and Healing. *Nat. Rev. Nephrol.* **2019**, *15* (9), 559–575. https://doi.org/10.1038/s41581-019-0163-2.

(16) Xu, J.; Zhang, X.; Monestier, M.; Esmon, N. L.; Esmon, C. T. Extracellular Histones Are Mediators of Death through TLR2 and TLR4 in Mouse Fatal Liver Injury. *J. Immunol.* **2011**, *187* (5), 2626–2631. https://doi.org/10.4049/jimmunol.1003930.

(17) Lood, C.; Blanco, L. P.; Purmalek, M. M.; Carmona-Rivera, C.; De Ravin, S. S.; Smith, C. K.; Malech, H. L.; Ledbetter, J. A.; Elkon, K. B.; Kaplan, M. J. Neutrophil Extracellular Traps Enriched in Oxidized Mitochondrial DNA Are Interferogenic and Contribute to Lupus-like Disease. *Nat. Med.* **2016**, *22* (2), 146–153. https://doi.org/10.1038/nm.4027.

(18) Radermecker, C.; Detrembleur, N.; Guiot, J.; Cavalier, E.; Henket, M.; Cataldo, D.; Delvenne, P.; Marichal, T.; Chemistry, M.; Biology, D. Neutrophil Extracellular Traps Infiltrate the Lung Vascular , Interstitial and Airway Compartments in Severe Covid-19. *J. Leukoc. Biol.* **2020**, *217* (12), 1–33.

(19) Zuo, Y.; Yalavarthi, S.; Shi, H.; Gockman, K.; Zuo, M.; Madison, J. A.; Blair, C.; Weber, A.; Barnes, B. J.; Egeblad, M.; et al. Neutrophil Extracellular Traps in COVID19. *J. Clin. Invest.* **2020**, *5* (11). https://doi.org/10.3390/cells9061494.

(20) Veras, F. P.; Pontelli, M.; Silva, C.; Toller-Kawahisa, J.; de Lima, M.; Nascimento, D.; Schneider, A.; Caetite, D.; Rosales, R.; Colon, D.; et al. SARS-CoV-2 Triggered Neutrophil Extracellular Traps (NETs) Mediate COVID-19 Pathology. *J. Exp. Med.* **2020**, *217* (12). https://doi.org/10.1101/2020.06.08.20125823.

(21) Middleton, E. A.; He, X.-Y.; Denorme, F.; Campbell, R. A.; Ng, D.; Salvatore, S. P.; Mostyka, M.; Baxter-Stoltzfus, A.; Borczuk, A. C.; Loda, M.; et al. Neutrophil Extracellular Traps (NETs) Contribute to Immunothrombosis in COVID-19 Acute Respiratory Distress

Syndrome. *Blood* **2020**, *136* (10). https://doi.org/10.1182/blood.2020007008.

(22) Veras, F.; et al. SARS-CoV-2 Triggered Neutrophil Extracellular Traps (NETs) Mediate COVID-19 Pathology. *MedRxiv* **2020**.

(23) Schönrich, G.; Raftery, M. J. Neutrophil Extracellular Traps Go Viral. *Front. Immunol.* **2016**, *7* (SEP), 11–14. https://doi.org/10.3389/fimmu.2016.00366.

(24) Thiam, H. R.; Wong, S. L. Cellular Mechanisms of NETosis. *Annu. Rev. Cell Dev. Biol.* **2020**, *8* (41), 1–28.

(25) Leshner, M.; Wang, S.; Lewis, C.; Zheng, H.; Chen, X. A.; Santy, L.; Wang, Y. PAD4 Mediated Histone Hypercitrullination Induces Heterochromatin Decondensation and Chromatin Unfolding to Form Neutrophil Extracellular Trap-like Structures. *Front. Immunol.* **2012**, *3* (October), 1–11. https://doi.org/10.3389/fimmu.2012.00307.

(26) Von Gunten, S.; Yousefi, S.; Seitz, M.; Jakob, S. M.; Schaffner, T.; Seger, R.; Takala, J.; Villiger, P. M.; Simon, H. U. Siglec-9 Transduces Apoptotic and Nonapoptotic Death Signals into Neutrophils Depending on the Proinflammatory Cytokine Environment. *Blood* **2005**, *106* (4), 1423–1431. https://doi.org/10.1182/blood-2004-10-4112.

(27) Angata, T.; Varki, A. Cloning, Characterization, and Phylogenetic Analysis of Siglec-9, a New Member of the CD33-Related Group of Siglecs: Evidence for Co-Evolution with Sialic Acid Synthesis Pathways. *J. Biol. Chem.* **2000**, *275* (29), 22127–22135. https://doi.org/10.1074/jbc.M002775200.

(28) Lizcano, A.; Secundino, I.; Dohrmann, S.; Corriden, R.; Rohena, C.; Diaz, S.; Ghosh, P.; Deng, L.; Nizet, V.; Varki, A. Erythrocyte Sialoglycoproteins Engage Siglec-9 on Neutrophils to Suppress Activation. *Blood* **2017**, *129* (23), 3100–3110. https://doi.org/10.1182/blood-2016-11-751636.

(29) Adams, O. J.; Stanczak, M. A.; von Gunten, S.; Läubli, H. Targeting Sialic Acid-Siglec Interactions to Reverse Immune Suppression in Cancer. *Glycobiology* **2017**, No. January 2018, 1–8. https://doi.org/10.1093/glycob/cwx108.

(30) Duan, S.; Paulson, J. C. Siglecs as Immune Cell Checkpoints in Disease. *Annu. Rev. Immunol.* **2020**, *38* (1), 365–395. https://doi.org/10.1146/annurev-immunol-102419-035900.

(31) Zhang, J. Q.; Nicoll, G.; Jones, C.; Crocker, P. R. Siglec-9, a Novel Sialic Acid Binding Member of the Immunoglobulin Superfamily Expressed Broadly on Human Blood Leukocytes. *J. Biol. Chem.* **2000**, *275* (29), 22121–22126. https://doi.org/10.1074/jbc.M002788200.

(32) Lizcano, A.; Secundino, I.; Dohrmann, S.; Corriden, R.; Rohena, C.; Diaz, S.; Ghosh, P.; Deng, L.; Nizet, V.; Varki, A. Erythrocyte Sialoglycoproteins Engage Siglec-9 on Neutrophils to Suppress Activation. *Blood* **2017**, *129* (23), 3100–3110. https://doi.org/10.1182/blood-2016-11-751636.

(33) Bornhöfft, K. F.; Galuska, S. P. Glycans as Modulators for the Formation and Functional Properties of Neutrophil Extracellular Traps : Used by the Forces of Good and Evil. *Front. Immunol.* **2019**, *10* (May), 1–9. https://doi.org/10.3389/fimmu.2019.00959.

(34) Carlin, A. F.; Uchiyama, S.; Chang, Y. C.; Lewis, A. L.; Nizet, V.; Varki, A. Molecular Mimicry of Host Sialylated Glycans Allows a Bacterial Pathogen to Engage Neutrophil Siglec-9 and Dampen the Innate Immune Response. *Blood* **2009**, *113* (14), 3333–3336. https://doi.org/10.1182/blood-2008-11-187302.

(35) Khatua, B.; Bhattacharya, K.; Mandal, C. Sialoglycoproteins Adsorbed by Pseudomonas Aeruginosa Facilitate Their Survival by Impeding Neutrophil Extracellular Trap through Siglec-9. *J. Leukoc. Biol.* **2012**, *91* (April), 641–655. https://doi.org/10.1189/jlb.0511260.

(36) Youngblood, B. A.; Brock, E. C.; Leung, J.; Falahati, R.; Bochner, B. S.; Rasmussen, H. S.; Peterson, K.; Bebbington, C.; Tomasevic, N. Siglec-8 Antibody Reduces Eosinophils and Mast Cells in a Transgenic Mouse Model of Eosinophilic Gastroenteritis. *JCI Insight* **2019**, *4* (19). https://doi.org/10.1172/jci.insight.126219.

(37) Tian, R. R.; Zhang, M. X.; Liu, M.; Fang, X.; Li, D.; Zhang, L.; Zheng, P.; Zheng, Y. T.; Liu, Y. CD24Fc Protects against Viral Pneumonia in Simian Immunodeficiency Virus-Infected Chinese Rhesus Monkeys. *Cell. Mol. Immunol.* **2020**, *17* (8), 887–888. https://doi.org/10.1038/s41423-020-0452-5.

(38) Tian, R. R.; Zhang, M. X.; Zhang, L. T.; Zhang, P.; Ma, J. P.; Liu, M.; Devenport, M.; Zheng, P.; Zhang, X. L.; Lian, X. D.; et al. CD24 and Fc Fusion Protein Protects SIVmac239-Infected Chinese Rhesus Macaque against Progression to AIDS. *Antiviral Res.* **2018**, *157* (June), 9–17. https://doi.org/10.1016/j.antiviral.2018.07.004.

(39) Chen, G. Y.; Tang, J.; Zheng, P.; Liu, Y. CD24 and Siglec-10 Selectively Repress Tissue Damage - Induced Immune Responses. *Science (80-.).* **2009**, *323* (5922), 1722–1725. https://doi.org/10.1126/science.1168988.

(40) Läubli, H.; Varki, A. Sialic Acid – Binding Immunoglobulin - like Lectins (Siglecs) Detect Self - Associated Molecular Patterns to Regulate Immune Responses. *Cell. Mol. Life Sci.* **2020**, *77* (4), 593–605. https://doi.org/10.1007/s00018-019-03288-x.

(41) Delaveris, C. S.; Chiu, S. H.; Riley, N. M.; Bertozzi, C. R. Modulation of Immune Cell Reactivity with Cis-Binding Siglec Agonists. *Proc. Natl. Acad. Sci.* No. In Press.

(42) Rillahan, C. D.; Schwartz, E.; McBride, R.; Fokin, V. V.; Paulson, J. C. Click and Pick: Identification of Sialoside Analogues for Siglec-Based Cell Targeting. *Angew. Chemie - Int. Ed.* **2012**, *51* (44), 11014–11018. https://doi.org/10.1002/anie.201205831.

(43) Hoppenbrouwers, T.; Autar, A. S. A.; Sultan, A. R.; Abraham, T. E.; Van Cappellen, W. A.; Houtsmuller, A. B.; Van Wamel, W. J. B.; Van Beusekom, H. M. M.; Van Neck, J. W.; De Maat, M. P. M. In Vitro Induction of NETosis: Comprehensive Live Imaging Comparison and Systematic Review. *PLoS One* **2017**, *12* (5), 1–29. https://doi.org/10.1371/journal.pone.0176472.

(44) Moreno-Eutimio, M. A.; López-Macías, C.; Pastelin-Palacios, R. Bioinformatic Analysis and Identification of Single-Stranded RNA Sequences Recognized by TLR7/8 in the SARS-CoV-2, SARS-CoV, and MERS-CoV Genomes. *Microbes Infect.* **2020**, *22* (4–5), 226–229. https://doi.org/10.1016/j.micinf.2020.04.009.

(45) Van Der Made, C. I.; Simons, A.; Schuurs-Hoeijmakers, J.; Van Den Heuvel, G.; Mantere, T.; Kersten, S.; Van Deuren, R. C.; Steehouwer, M.; Van Reijmersdal, S. V.; Jaeger, M.; et al. Presence of Genetic Variants among Young Men with Severe COVID-19. *J. Am. Med. Assoc.* **2020**, *324* (7), 663–673. https://doi.org/10.1001/jama.2020.13719.

(46) Gupta, S.; Chan, D. W.; Zaal, K. J.; Kaplan, M. J. A High-Throughput Real-Time Imaging Technique To Quantify NETosis and Distinguish Mechanisms of Cell Death in Human Neutrophils. *J. Immunol.* **2018**, *200* (2), 869–879. https://doi.org/10.4049/jimmunol.1700905.

(47) Zecha, J.; Satpathy, S.; Kanashova, T.; Avanessian, S. C.; Kane, M. H.; Clauser, K. R.; Mertins, P.; Carr, S. A.; Kuster, B. TMT Labeling for the Masses: A Robust and Cost-Efficient, in-Solution Labeling Approach. *Mol. Cell. Proteomics* **2019**, *18* (7), 1468–1478. https://doi.org/10.1074/mcp.TIR119.001385.

(48) Lood, C.; Arve, S.; Ledbetter, J.; Elkon, K. B. TLR7 / 8 Activation in Neutrophils Impairs Immune Complex Phagocytosis through Shedding of FcgRIIA. *J. Exp. Med.* **2017**, *214* (7), 2103–2119.

(49) Zhu, X.; Chen, J. Phosphoproteomic Analyses Provide Insight into Molecular Mechanisms Underlying NETosis. *Proteomics* **2019**, *19*, 1900126. https://doi.org/10.1002/pmic.201900126.

(50) Delaveris, C. S.; Webster, E. R.; Banik, S. M.; Boxer, S. G.; Bertozzi, C. R. Membrane-Tethered Mucin-like Polypeptides Sterically Inhibit Binding and Slow Fusion Kinetics of Influenza A Virus. *Proc. Natl. Acad. Sci.* **2020**, *117* (23), 12643–12650.

(51) Stanczak, M. A.; Zippelius, A.; Läubli, H. Self-Associated Molecular Patterns Mediate Cancer Immune Evasion by Engaging Siglecs on T Cells Graphical Abstract Find the Latest Version : *J Clin. Investig.* **2018**. https://doi.org/10.1172/JCI120612.

(52) Läubli, H.; Pearce, O. M. T.; Schwarz, F.; Siddiqui, S. S.; Deng, L.; Stanczak, M. A. Engagement of Myelomonocytic Siglecs by Tumor-Associated Ligands Modulates the Innate Immune Response to Cancer. **2014**, *111* (39), 1–6. https://doi.org/10.1073/pnas.1409580111.

(53) Baskin, J. M.; Wu, X.; Christiano, R.; Oh, M. S.; Schauder, C. M.; Gazzerro, E.; Messa, M.; Baldassari, S.; Assereto, S.; Biancheri, R.; et al. The Leukodystrophy Protein FAM126A (Hyccin) Regulates PtdIns(4)P Synthesis at the Plasma Membrane. *Nat. Cell Biol.* **2016**, *18* (1). https://doi.org/10.1038/ncb3271.

(54) Phan, T. K.; Williams, S. A.; Bindra, G. K.; Lay, F. T.; Poon, I. K. H.; Hulett, M. D. Phosphoinositides : Multipurpose Cellular Lipids with Emerging Roles in Cell Death. *Cell Death Differ.* **2019**, *26*, 781–793. https://doi.org/10.1038/s41418-018-0269-2.

(55) Saito, S.; Kawamura, T.; Higuchi, M.; Kobayashi, T.; Yoshita-takahashi, M.; Yamazaki, M.; Abe, M.; Sakimura, K.; Kanda, Y.; Kawamura, H.; et al. RASAL3 , a Novel Hematopoietic RasGAP Protein , Regulates the Number and Functions of NKT Cells. *Eur. J. Immunol.* **2015**, *45*, 1512–1523. https://doi.org/10.1002/eji.201444977.

(56) Moghanloo, E.; Ghorbani, E.; Beikverdi, M. S.; Badameh, P.; Rezaei, S.; Piroozmand, A.; Teimourian, S.; Shahidi, M.; Khorshidi, A. The Netosis Formation of HL-60 Cell Differentiated to Neutrophil-Like Cells by LPS. *J. Human, Environ. Heal. Promot.* **2018**, *4* (3), 138–143. https://doi.org/10.29252/jhehp.4.3.8.

(57) Meizlish, M. L.; Pine, A. B.; Bishai, J. D.; Goshua, G.; Nadelmann, E. R.; Simonov, M.; Chang, C.-H.; Zhang, H.; Shallow, M.; Bahel, P.; et al. A Neutrophil Activation Signature Predicts Critical Illness and Mortality in COVID-19. *medRxiv Prepr. Serv. Heal. Sci.* **2020**, *06510*. https://doi.org/10.1101/2020.09.01.20183897.

(58) Quinn, M. T.; Editors, F. R. D. *Neutrophil: Methods and Protocols*, Third.; Springer Science: New York, 2020.

(59) Branitzki-Heinemann, K.; Möllerherm, H.; Völlger, L.; Husein, D. M.; de Buhr, N.; Blodkamp, S.; Reuner, F.; Brogden, G.; Naim, H. Y.; Von Köckritz-Blickwede, M. Formation of Neutrophil Extracellular Traps under Low Oxygen Level. *Front. Immunol.* **2016**, *7* (NOV), 1–9. https://doi.org/10.3389/fimmu.2016.00518.

(60) Grasso, S.; Neumann, A.; Lang, I. M.; Etscheid, M.; von Köckritz-Blickwede, M.; Kanse, S. M. Interaction of Factor VII Activating Protease (FSAP) with Neutrophil Extracellular Traps (NETs). *Thromb. Res.* **2018**, *161* (September 2017), 36–42. https://doi.org/10.1016/j.thromres.2017.11.012.

(61) Fuchs, T. A.; Brill, A.; Duerschmied, D.; Schatzberg, D.; Monestier, M.; Myers, D. D.; Wrobleski, S. K.; Wakefield, T. W.; Hartwig, J. H.; Wagner, D. D. Extracellular DNA Traps Promote Thrombosis. *Proc. Natl. Acad. Sci. U. S. A.* **2010**, *107* (36), 15880–15885. https://doi.org/10.1073/pnas.1005743107.

(62) Perdomo, J.; Leung, H. H. L.; Ahmadi, Z.; Yan, F.; Chong, J. J. H.; Passam, F. H.; Chong, B. H. Neutrophil Activation and NETosis Are the Major Drivers of Thrombosis in

Heparin-Induced Thrombocytopenia. *Nat. Commun.* **2019**, *10* (1), 1–14. https://doi.org/10.1038/s41467-019-09160-7.

(63) Warnatsch, A.; Ioannou, M.; Wang, Q.; Papayannopoulos, V. Neutrophil Extracellular Traps License Macrophages for Cytokine Production in Atherosclerosis. *Science (80-.).* **2015**, *349* (6245), 1–6.

(64) Papayannopoulos, V.; Staab, D.; Zychlinsky, A. Neutrophil Elastase Enhances Sputum Solubilization in Cystic Fibrosis Patients Receiving DNase Therapy. **2011**, *6* (12), 1–7. https://doi.org/10.1371/journal.pone.0028526.

(65) Büll, C.; Heise, T.; Beurskens, D. M. H.; Riemersma, M.; Ashikov, A.; Rutjes, F. P. J. T.; Van Kuppevelt, T. H.; Lefeber, D. J.; Den Brok, M. H.; Adema, G. J.; et al. Sialic Acid Glycoengineering Using an Unnatural Sialic Acid for the Detection of Sialoglycan Biosynthesis Defects and On-Cell Synthesis of Siglec Ligands. *ACS Chem. Biol.* **2015**, *10* (10), 2353–2363. https://doi.org/10.1021/acschembio.5b00501.

(66) Manda-Handzlik, A.; Bystrzycka, W.; Wachowska, M.; Sieczkowska, S.; Stelmaszczyk-Emmel, A.; Demkow, U.; Ciepiela, O. The Influence of Agents Differentiating HL-60 Cells toward Granulocyte-like Cells on Their Ability to Release Neutrophil Extracellular Traps. *Immunol. Cell Biol.* **2018**, *96* (4), 413–425. https://doi.org/10.1111/imcb.12015.

(67) HaileMariam, M.; Eguez, R. V.; Singh, H.; Bekele, S.; Ameni, G.; Pieper, R.; Yu, Y. S-Trap, an Ultrafast Sample-Preparation Approach for Shotgun Proteomics. *J. Proteome Res.* **2018**, *17* (9), 2917–2924. https://doi.org/10.1021/acs.jproteome.8b00505.

(68) Brenes, A.; Hukelmann, J.; Bensaddek, D.; Lamond, A. I. Multibatch TMT Reveals False Positives, Batch Effects and Missing Values. *Mol. Cell. Proteomics* **2019**, *18* (10), 1967–1980. https://doi.org/10.1074/mcp.RA119.001472.

(69) Hebert, A. S.; Thöing, C.; Riley, N. M.; Kwiecien, N. W.; Shiskova, E.; Huguet, R.; Cardasis, H. L.; Kuehn, A.; Eliuk, S.; Zabrouskov, V.; et al. Improved Precursor Characterization for Data-Dependent Mass Spectrometry. *Anal. Chem.* **2018**, *90* (3), 2333–2340. https://doi.org/10.1021/acs.analchem.7b04808.

(70) Zhou, H.; Ye, M.; Dong, J.; Corradini, E.; Cristobal, A.; Heck, A. J. R.; Zou, H.; Mohammed, S. Robust Phosphoproteome Enrichment Using Monodisperse Microsphere-Based Immobilized Titanium (IV) Ion Affinity Chromatography. *Nat. Protoc.* **2013**, *8* (3), 461–480. https://doi.org/10.1038/nprot.2013.010.

(71) Cox, J.; Neuhauser, N.; Michalski, A.; Scheltema, R. A.; Olsen, J. V; Mann, M. Andromeda: A Peptide Search Engine Integrated into the MaxQuant Environment. *J. Proteome Res.* **2011**, *10* (4), 1794–1805. https://doi.org/10.1021/pr101065j.

(72) Tyanova, S.; Temu, T.; Cox, J. The MaxQuant Computational Platform for Mass Spectrometry-Based Shotgun Proteomics. *Nat. Protoc.* **2016**, *11* (12), 2301–2319. https://doi.org/10.1038/nprot.2016.136.

(73) Bateman, A. UniProt: A Worldwide Hub of Protein Knowledge. *Nucleic Acids Res.* **2019**, *47* (D1), D506–D515. https://doi.org/10.1093/nar/gky1049.

(74) Tyanova, S.; Temu, T.; Sinitcyn, P.; Carlson, A.; Hein, M. Y.; Geiger, T.; Mann, M.; Cox, J. The Perseus Computational Platform for Comprehensive Analysis of (Prote)Omics Data. *Nat. Methods* **2016**, *13* (9), 731–740. https://doi.org/10.1038/nmeth.3901.

(75) Perez-Riverol, Y.; Csordas, A.; Bai, J.; Bernal-Llinares, M.; Hewapathirana, S.; Kundu, D. J.; Inuganti, A.; Griss, J.; Mayer, G.; Eisenacher, M.; et al. The PRIDE Database and Related Tools and Resources in 2019: Improving Support for Quantification Data. *Nucleic Acids Res.* **2019**, *47* (D1), D442–D450. https://doi.org/10.1093/nar/gky1106.

(76) Stuart, T.; Butler, A.; Hoffman, P.; Hafemeister, C.; Papalexi, E.; Mauck, W. M.; Hao, Y.; Stoeckius, M.; Smibert, P.; Satija, R. Comprehensive Integration of Single-Cell Data. *Cell* **2019**, *177* (7), 1888-1902.e21. https://doi.org/10.1016/j.cell.2019.05.031.

Supplementary Figures.

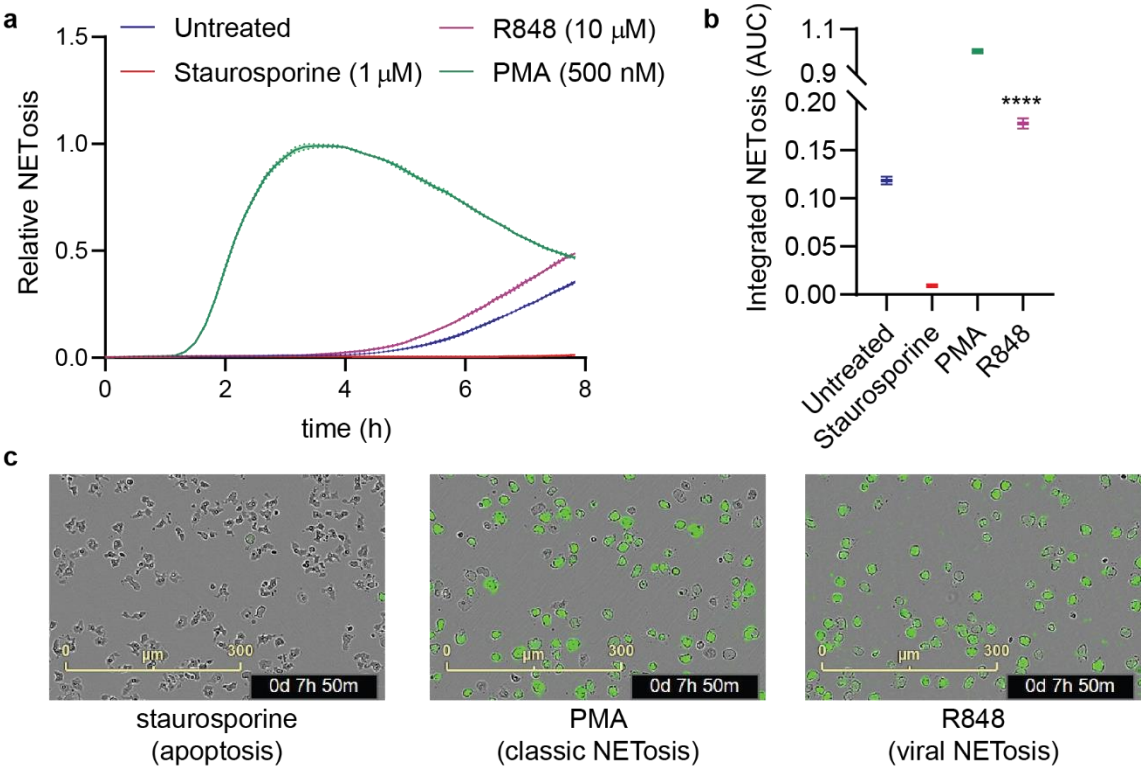

Figure S1.TLR-7/8 agonist R848 induces NETosis in primary neutrophils. (**a-c**) Primary neutrophils were treated with compounds at the concentrations detailed in (**a**) in IMDM supplemented 0.5% hiFBS containing the membrane impermeable DNA intercalator Cytotox Green (250 nM). Images were acquired by fluorescence microscopy every 10 min for 8 h. The area of all green fluorescent objects >300 μm^2 was quantified and averaged across three images per well. Relative NETosis was determined by normalizing to the maximal NET area from PMA treatment (t = 3 h). (**a**) Time-course data for NET formation and degradation over time. Error bands represent SEM. (**b**) Quantitation of (**a**) as area under the curve. Error bars represent SD. All data are representative of multiple independent experiments using neutrophils from different donors. **** $p < 0.0001$. (**c**) Representative images of neutrophils treated with staurosporine, PMA, or R848 stained with Cytotox Green at t = 7h 50m.

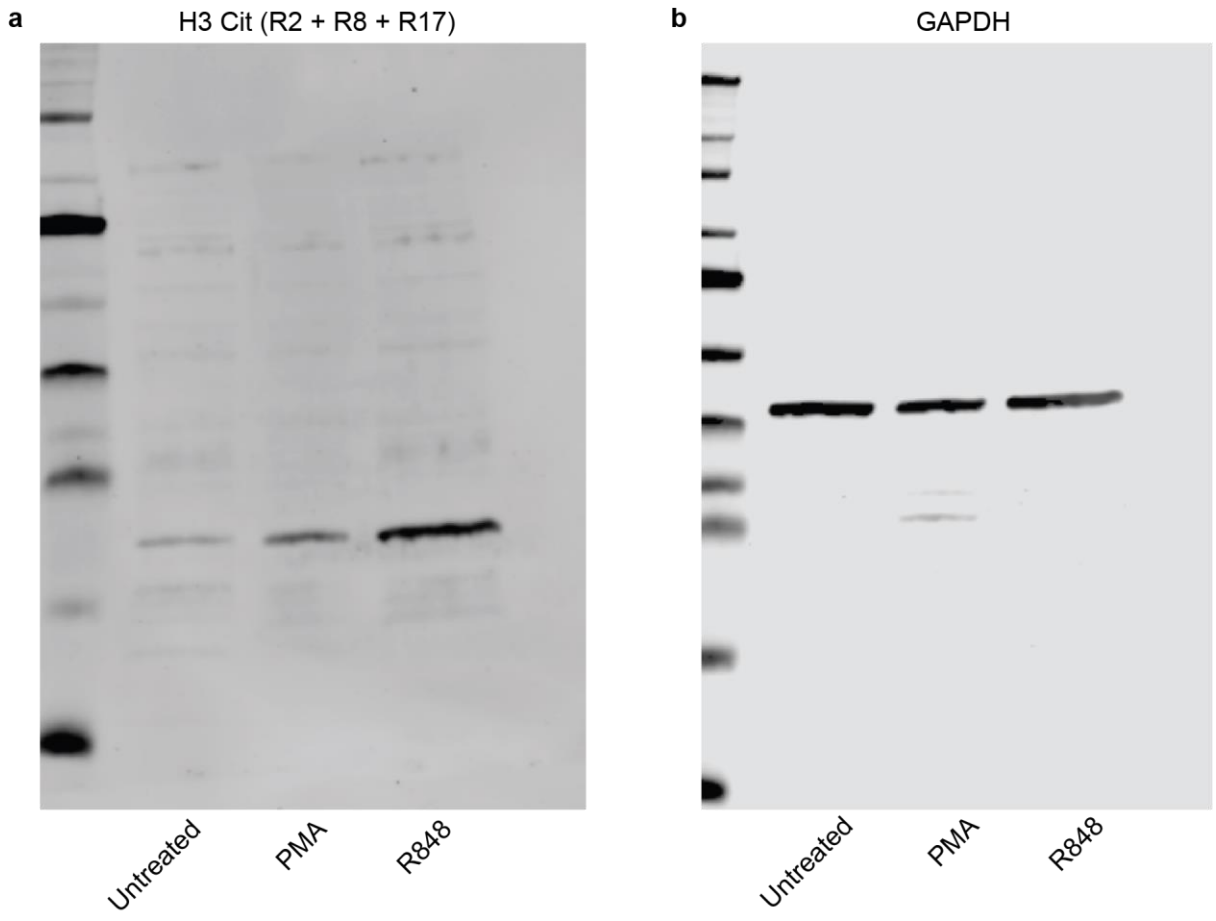

Figure S2. R848 induces rapid citrullination of H3 in primary neutrophils. Primary neutrophils were treated with compound in IMDM [+] 0.5% hiFBS for 30 min before being lysed and analyzed by Western blot for citrullination of histone H3. (**a**) H3Cit (R2 + R8 + R17). (**b**) GAPDH.

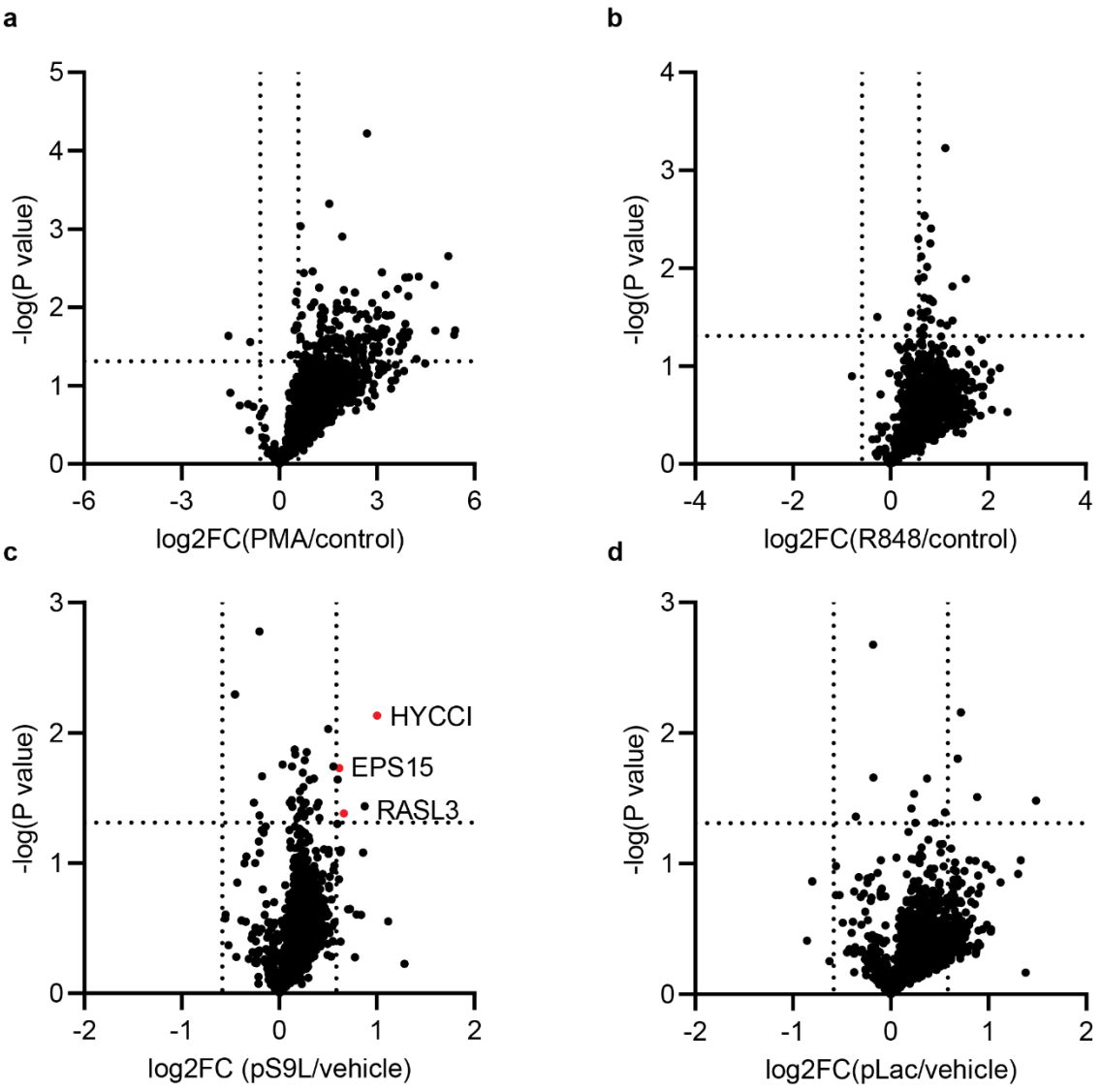

Figure S3. Volcano plots of significance vs. fold-change for phosphopeptides enriched from neutrophil lysates. Neutrophils isolated from healthy donor whole blood were treated with either PMA (500 nM) or R848 (10 µM) or left untreated for 30 min (**a**,**b**) or with R848 (10 µM) and one of pS9L (500 nM), pLac (500 nM) or vehicle for 15 min (**c**,**d**) in IMDM [+] 0.5% hiFBS. The cells were lysed, digested, and phosphopeptides were enriched before being TMT-labeled and analyzed by LC-MS. Vertical lines represent x = +/- 0.585 (corresponding to 1.5-fold change) and horizontal lines represent p = 0.05 as determined by a paired t-test to account for variability between neutrophil donors. Each datapoint represents the average fold-change from three

different donors. (**a**) Fold-change of PMA compared to untreated neutrophils. (**b**) Fold-change of R848 compared to untreated neutrophils. (**c**) Fold-change of pS9L-treated compared to vehicle-treated R848-stimualted neutrophils. Red dots highlight significant hits unique to this dataset compared to (**d**). (**d**) Fold-change of pLac-treated compared to vehicle-treated R848-stimualted neutrophils.

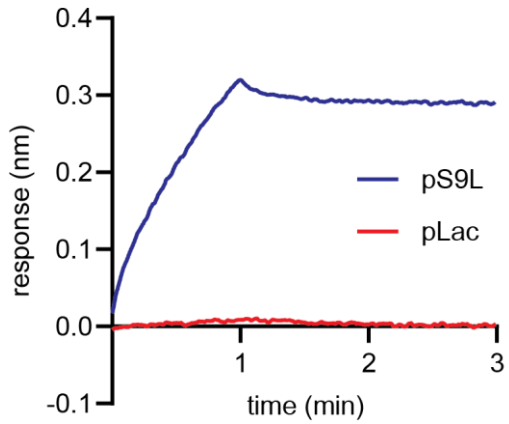

Figure S4. Siglec-9 binds pS9L but not pLac. Siglec-9-Fc was immobilized onto anti-hFc-coated tips on an OctetRed96 to a threshold of 0.4 nm. Association of glycopolypeptide (2.5 μM) was measured by dipping Siglec-9-Fc coated tips into a solution of glycopolypeptide in PBS with 0.1% BSA to abrogate nonspecific binding. Tips were conditioned prior to the first assay and regenerated between runs with three washes in 100 mM glycine buffer (pH 1.5).

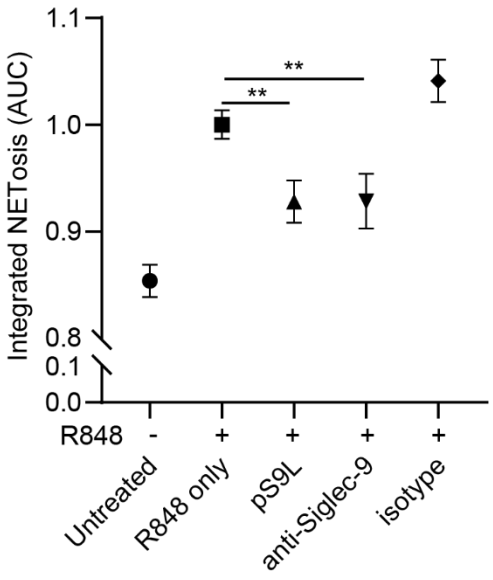

Figure S5. pS9L inhibits NETosis comparably to Siglec-9 agonist antibody. Primary neutrophils were cotreated with R848 (10 µM) and either cis-binding Siglec-9 agonist pS9L (500 nM) or antibody (anti-Siglec-9 clone 191240 or an isotype control IgG) (35 µg/mL) precomplexed with Protein A (5 µg/mL) or vehicle in IMDM supplemented with 0.5% hiFBS and containing Cytotox Green (250 nM). Images were acquired by fluorescence microscopy on an Incucyte Zoom every 1 h for 12 h. The area of all green fluorescent objects >200 μm^2 was quantified and averaged across three images per well. The area under the curve was quantified and normalized to the mean value for R848 treated neutrophils with no cotreatment.

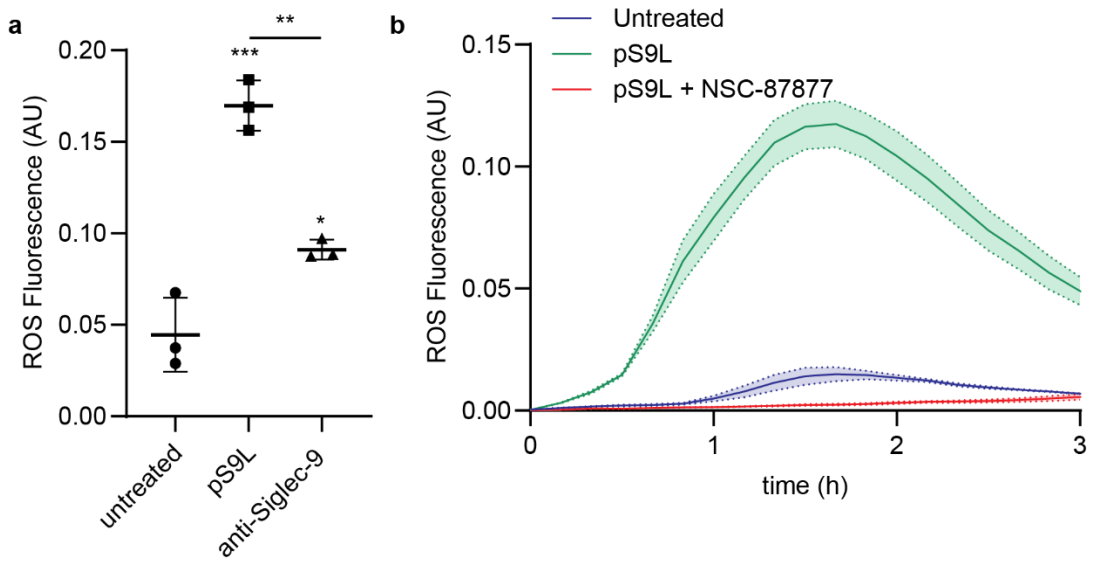

Figure S6. Siglec-9 engagement induces a SHP-1/2 dependent oxidative burst. (**a**) Primary neutrophils were treated with either cis-binding Siglec-9 agonist pS9L (500 nM) or anti-Siglec-9 (clone 191240) (35 µg/mL) precomplexed with Protein A (5 µg/mL) or vehicle in IMDM supplemented with 0.5% hiFBS and containing CellROX Deep Red (5 µM). Phase and red fluorescence images were acquired every 10 min using an Incucyte S3 in a 37 °C and 5% CO_2 incubator. ROS fluorescence was quantitated using integrated intensity normalized to confluence. Statistics were determined by one-way ANOVA. * = $p < 0.05$; ** = $p < 0.01$; *** = $p < 0.001$. (**b**) As in (**a**), with or without the SHP-1/2 inhibitor NSC-87877 (50 µM), as has been previously used to study SHP-1/2-mediated Siglec activity.[65]

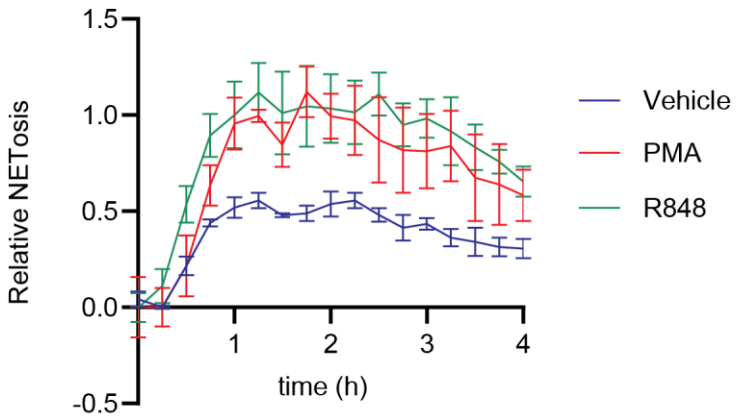

Figure S7. TLR-7/8 agonist R848 induces NETosis in dHL-60 cells. HL-60 cells were cultured in RPMI-1640 supplemented with 20% hiFBS in the presence of DMSO (1.25% v/v) and ATRA (100 nM) for 6 d. Cells were then seeded in serum-free RPMI-1640 containing Cytotox Green (250 nM) and NETosis was induced with PMA (100 nM), R848 (10 µM), or vehicle. Phase and green fluorescence images were acquired every 15 min using an Incucyte S3. The area of all green fluorescent objects >200 μm^2 was quantified and averaged across three images per well. Relative NETosis was determined by normalizing to the maximal NET area from PMA treatment alone (t = 2.5 h).

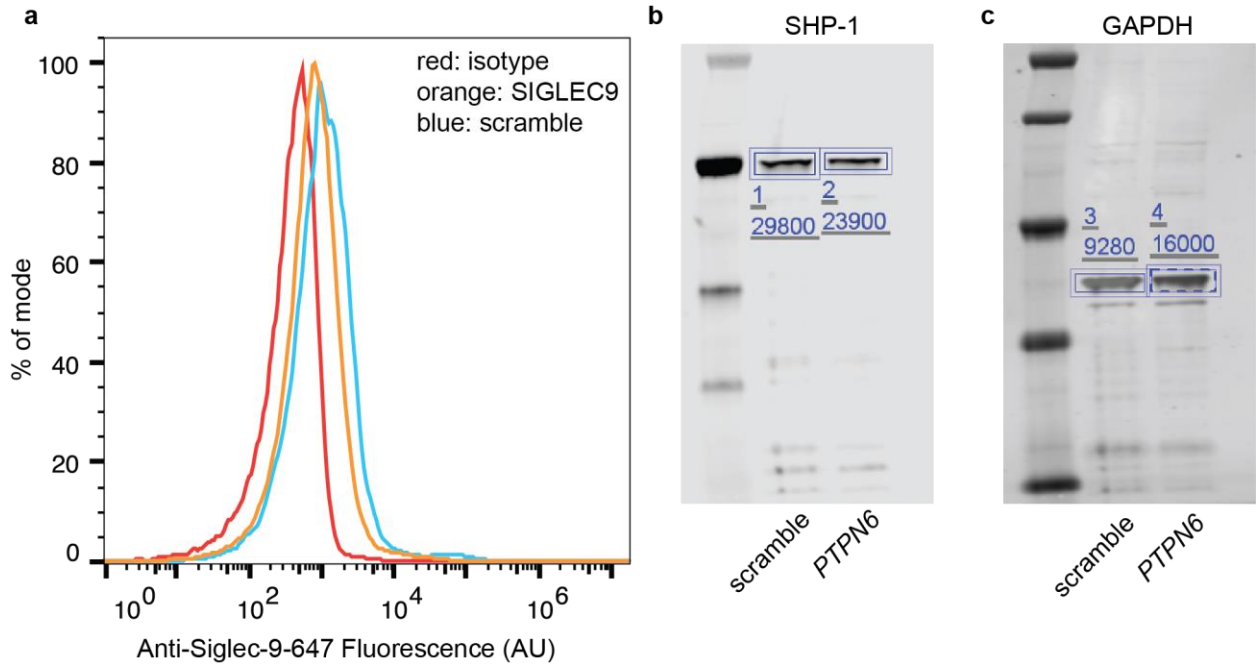

670

671 **Figure S8.** Siglec-9 and SHP-1 levels are reduced by siRNA knock-down of differentiated HL-
672 60 neutrophil-like cells. HL-60 cells were cultured in RPMI-1640 supplemented with 20% hiFBS
673 in the presence of DMSO (1.25% v/v) and ATRA (100 nM). After 4 d, the media was changed
674 and cells were treated with siRNA's. On day 6, expression of target proteins was assayed. (**a**)
675 dHL-60's treated with either SIGLEC9-targeting or scramble siRNA's were stained with an anti-
676 Siglec-9 antibody (clone K8, AlexaFluor647 conjugate) or an isotype control and analyzed by
677 flow cytometry. (**b**,**c**) Lysates from dHL-60's treated with siRNA's targeting PTPN6 (encoding
678 SHP-1) or a scrambled negative control were analyzed by Western blot, staining for either SHP-
679 1 (**b**) or GAPDH (**c**). Fluorescence signal was quantitated by LiCOR.

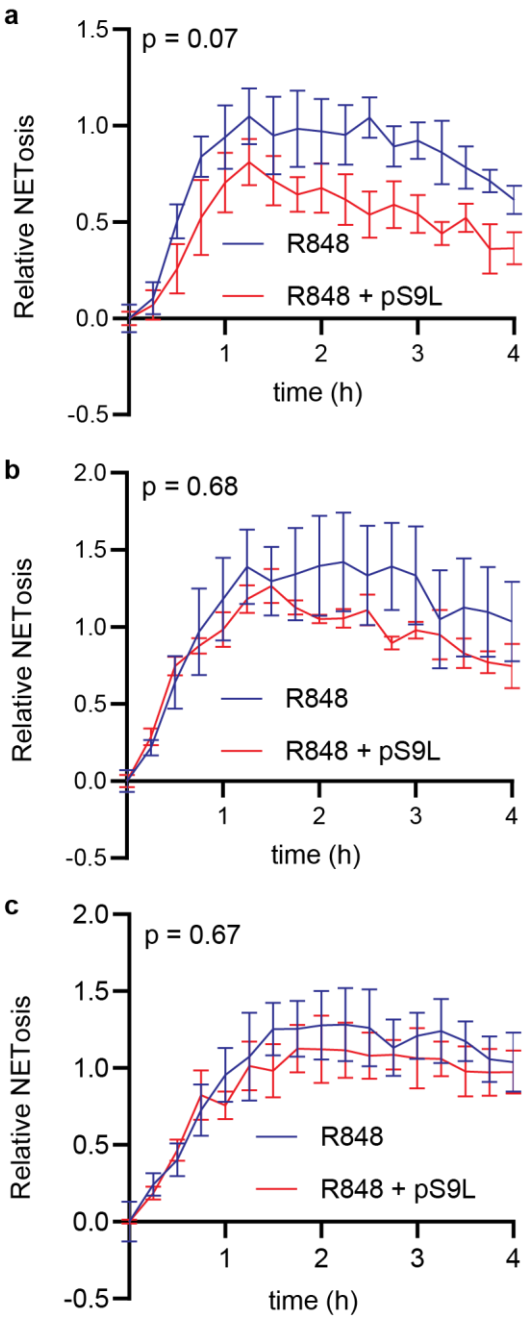

680

681 **Figure S9.** Cis Siglec-9 agonist pS9L inhibits NETosis via Siglec-9 and SHP-1. HL-60 cells
682 were cultured in RPMI-1640 supplemented with 20% hiFBS in the presence of DMSO (1.25%
683 v/v) and ATRA (100 nM). After 4 d, the media was changed and cells were treated with siRNA's.
684 On day 6, cells were then seeded in serum-free RPMI-1640 containing Cytotox Green (250 nM)
685 and NETosis was induced with R848 (10 µM) with or without pS9L (500 nM). Phase and green

686 fluorescence images were acquired every 15 min using an Incucyte S3. The area of all green
687 fluorescent objects >200 μm^2 was quantified and averaged across three images per well.
688 Relative NETosis was determined by normalizing to the maximal NET area from PMA treatment
689 alone (t = 2.5 h). (**a**) Scramble siRNA control. (**b**) SIGLEC9 targeting siRNA cocktail. (**c**) PTPN6
690 siRNA. Statistics were calculated by two-way ANOVA.

691

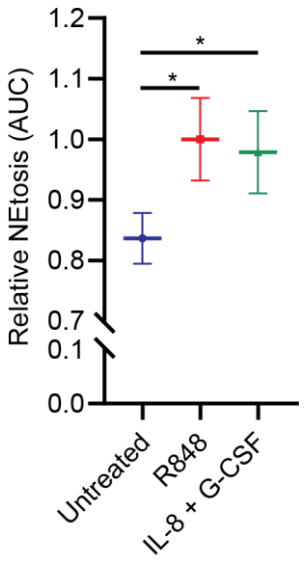

692

693 **Figure S10.** A combination of IL-8 and G-CSF induce NETosis in primary neutrophils. Primary
694 neutrophils were stimulated with R848 (10 µM), a combination of IL-8 (100 ng/mL) and G-CSF
695 (100 ng/mL), or vehicle and cultured in IMDM supplemented 0.5% hiFBS containing the
696 membrane impermeable DNA intercalator Cytotox Green (250 nM). Images were acquired by
697 fluorescence microscopy every 1 h for 8 h. The area of all green fluorescent objects >300 μm^2
698 was quantified and averaged across three images per well. Data were quantitated as area
699 under the curve measurements. Error bars represent SD. Data are representative of multiple
700 independent experiments using neutrophils from different donors. * $p < 0.05$.

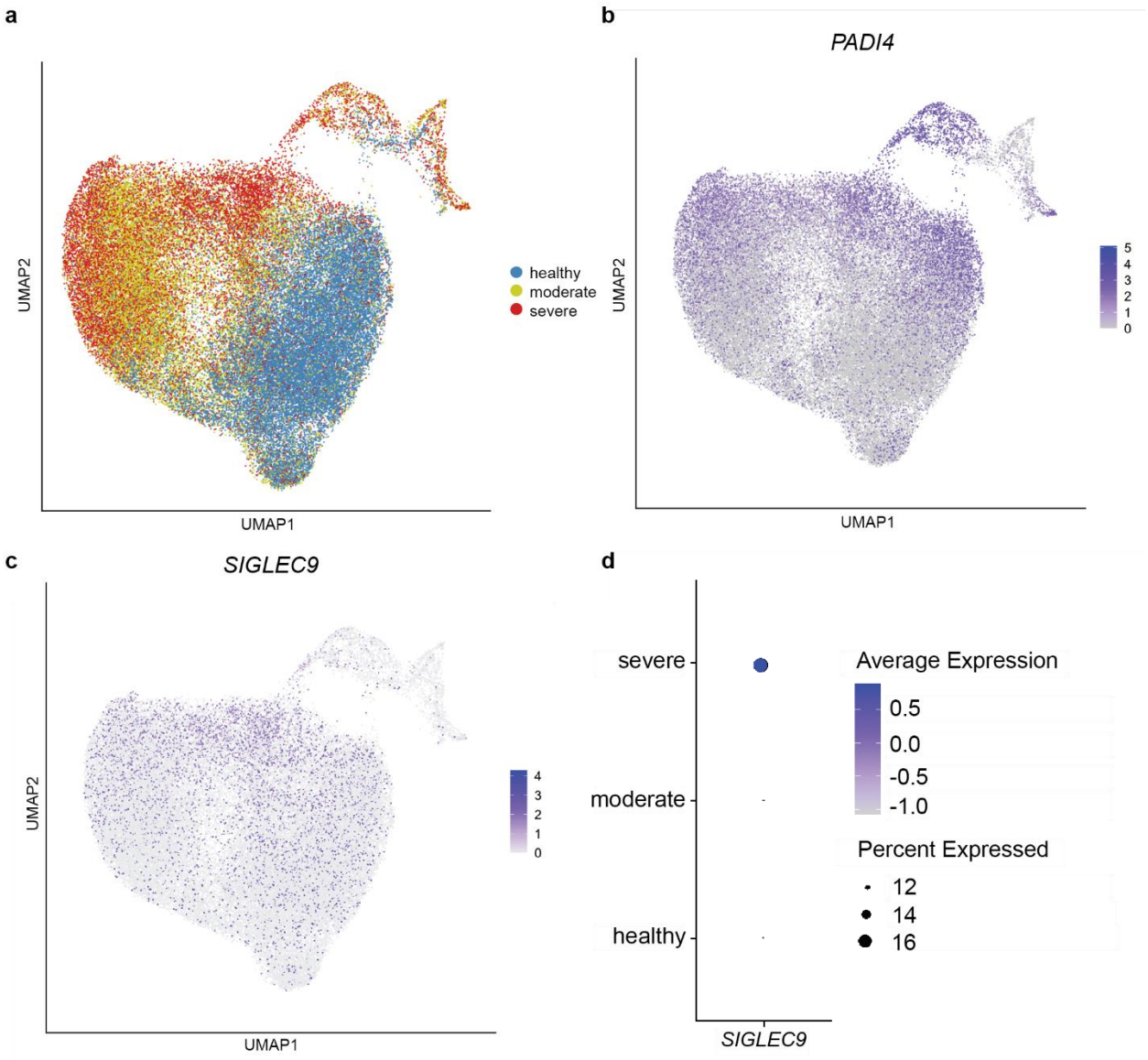

Figure S11. *SIGLEC9* and *PADI4* are upregulated by neutrophils of patients with severe COVID-19. (**a-c**) Uniform Manifold Approximation and Projection (UMAP) plot of neutrophils from the single-cell transcriptomic dataset published by Schulte-Schrepping and coworkers.[8] (**a**) Each cell is colored by the WHO severity score class (moderate, WHO score 4-5; severe, WHO score 6-8) of the patient at the time of sample collection, demonstrating strong severity-associated phenotypic reconfiguration of neutrophil transcriptome in COVID-19. (**b**) Each cell is colored by relative *PADI4* expression. (**c**) Each cell is colored by relative *SIGLEC9* expression.

(**d**) Dot plot depicting average and percent *SIGLEC9* expression by neutrophils in each WHO severity score class, indicating upregulation of *SIGLEC9* in severe COVID-19.

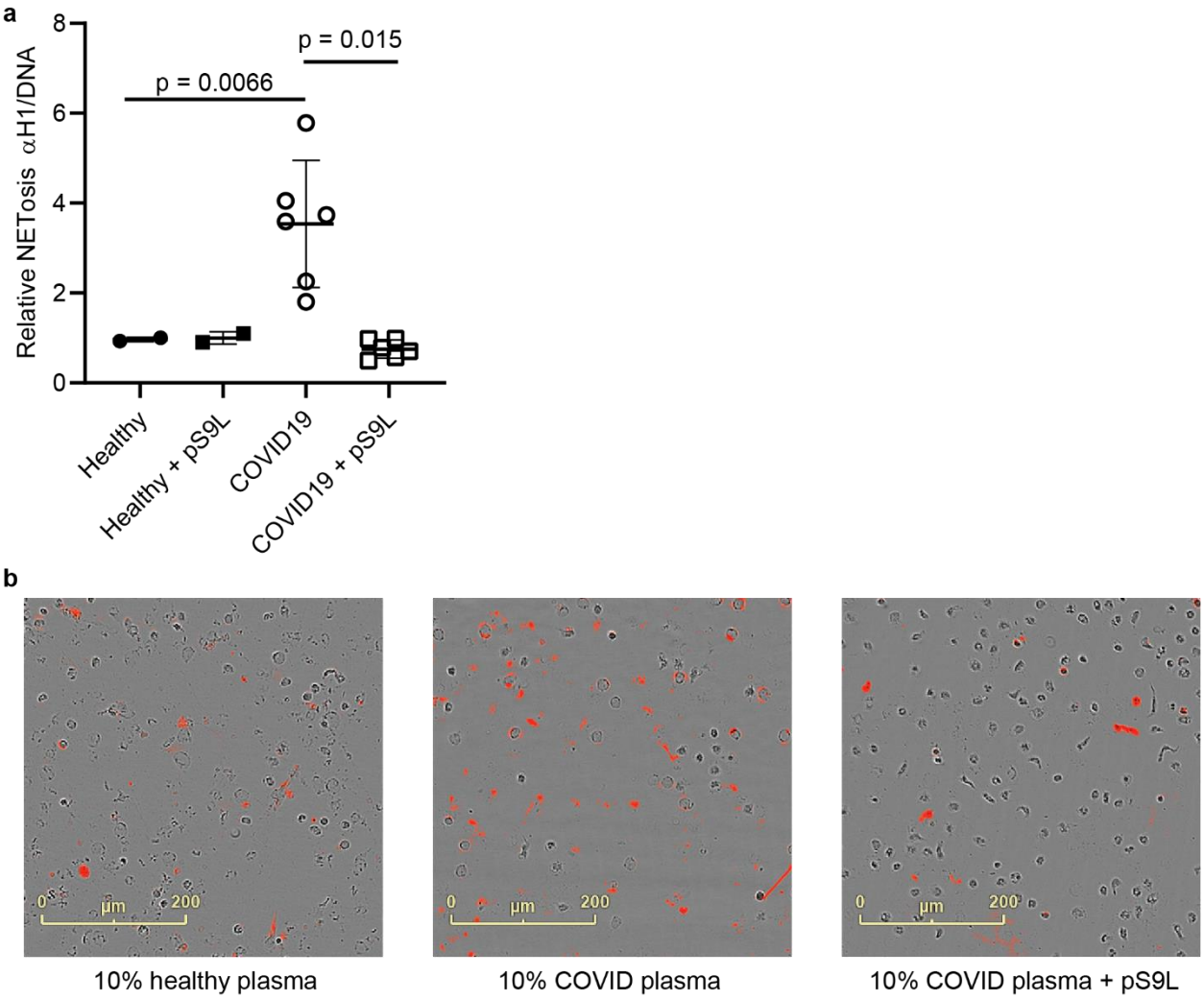

Figure S12. A Siglec-9 agonist inhibits NETosis of neutrophils induced by 10% COVID-19 plasma diluted in media. Neutrophils were isolated from healthy donors and cultured with pS9L (500 nM) in undiluted plasma for 4 h. Plasma was citrate anti-coagulated and from healthy donors or COVID-19 patients and diluted to 10% in IMDM. Cells were then fixed with 4% paraformaldehyde and blocked in 10% goat serum without permeabilization. (**a**) NETs were detected by immunocytochemistry with a mouse anti-H1/DNA complex primary antibody (MAB3864, 1:100) and a goat anti-mouse AlexaFluor594 (1:1000) secondary. Cells were counterstained with MemGlow488 prior to imaging but after immunostaining. The area of all red fluorescent objects >25 µm^2 and >2.0 RCU was quantified and averaged across four images per

well for three wells and normalized to cell count as determined by green fluorescent objects >50 μm^2 and >10.0 GCU. Each data point represents the mean value from technical replicates of an individual donor/patient. Error bars represent SD. Statistics were determined using a mixed effects model to account for differences in neutrophil donors and paired for matched patient plasmas. (**b**) Representative images showing anti-H1/DNA staining.

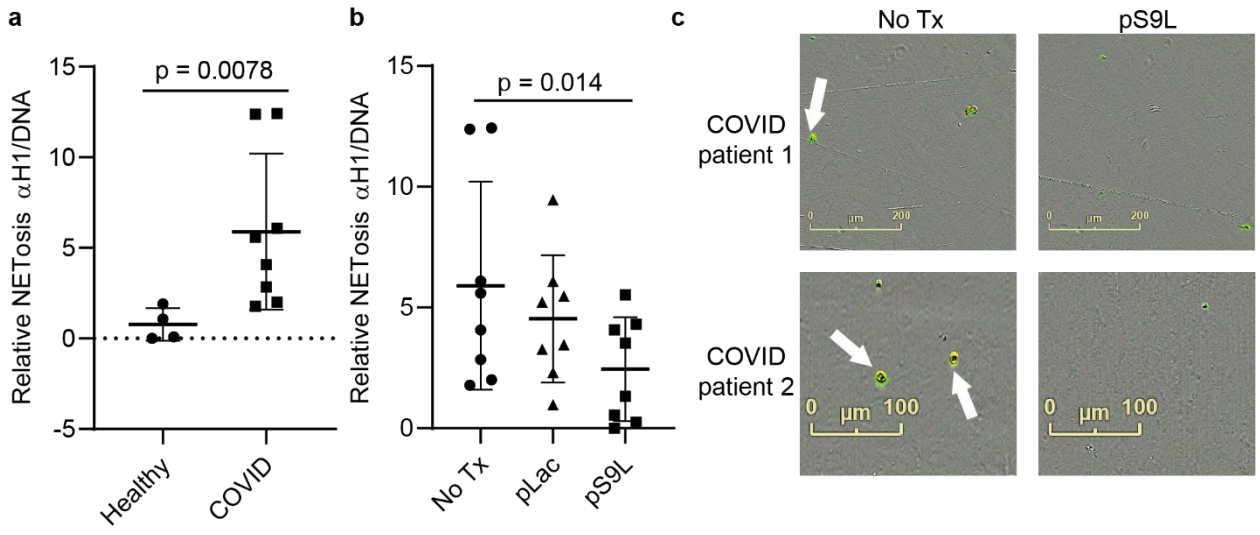

729

730 **Figure S13**. A Siglec-9 agonist inhibits NETosis of neutrophils induced by undiluted COVID-19
731 plasma. Neutrophils were isolated from healthy donors and cultured with pS9L (500 nM) or pLac
732 (500 nM) in undiluted plasma for 4 h. Plasma was citrate anti-coagulated and from healthy
733 donors or COVID-19 patients. Cells were then fixed with 4% paraformaldehyde and blocked in
734 10% goat serum without permeabilization. (**a**) NETs were detected by immunocytochemistry
735 with a mouse anti-H1/DNA complex primary antibody (MAB3864, 1:100) and a goat anti-mouse
736 AlexaFluor594 (1:1000) secondary. Cells were counterstained with MemGlow488 prior to
737 imaging but after immunostaining. The area of all red fluorescent objects >25 µm^2 and >2.0
738 RCU was quantified and averaged across four images per well for three wells and normalized to
739 cell count as determined by green fluorescent objects >50 µm^2 and >10.0 GCU. Each data point
740 represents the mean value from technical replicates of an individual donor/patient. Error bars
741 represent SD. Statistics were determined using a mixed effects model to account for differences
742 in neutrophil donors and paired for matched patient plasmas. (**b**) Representative images
743 showing anti-H1/DNA staining (red) overlayed with MemGlow488 (green).

744

745

Materials and Methods.

Glycopolypeptide synthesis.

Glycopolypeptides were synthesized as previously described.[41,50] In brief, *N*-carboxyanhydride monomers were polymerized either with a functionalized initiator that affords a membrane-tethering moiety or with a Ni(0) initiator that affords a soluble polypeptide. Polypeptides were deprotected with hydrazine monohydrate and purified by dialysis. In some cases, lactose-bearing scaffolds were then chemoenzymatically functionalized to afford terminal Siglec-9 ligands.[41] All glycopolypeptides were endotoxin purified on Pierce endotoxin removal resin (ThermoFisher, 88274) and sterile filtered (0.22 μm) before use.

Primary cell isolation.

Whole blood samples were obtained from the healthy donors and anti-coagulated with K2EDTA at the Stanford Blood Center. Samples were de-identified by the Stanford Blood Center. Neutrophils were purified on the same day as isolation, and the whole blood samples were kept at room temperature between collection and neutrophil isolation. Neutrophils were isolated by EasySep Direct Neutrophil Isolation Kit (StemCell Technologies, 19666) according to the manufacturer's instructions in 5 mL aliquots on a magnetized rack (StemCell Technologies, 18103). Efficiency of isolation was determined by flow cytometry to identify CD45 and CD14 hi cells. Neutrophils were routinely obtained in >96% purity via this method.

COVID-19 patients and specimen collection.

Peripheral blood was collected from patients enrolled in the IRB-approved Stanford University Emergency Department COVID-19 Biobank beginning in April 2020 after written informed

consent from patients or their surrogates. Eligibility criteria included age ≥18 years and presentation to the Stanford Hospital with a positive SARS-CoV-2 nasopharyngeal swab by RT-PCR. Patients were phenotyped for COVID-19 severity according to the universal World Health Organization (WHO) ordinal scale. Blood draws from patients occurred upon presentation to the Stanford Hospital Emergency Department in concert with usual care to avoid unnecessary personal protective equipment usage. Blood was collected into CPT vacutainers (Becton, Dickinson, and Co.) and plasma isolated, aliquoted, and stored at -80°C after centrifugation at 1800 x g for 20 minutes at 25°C. All sample processing occurred under BSL2+ biosafety precautions as approved by Stanford University APB.

Cell culture.

The acute promyelocytic leukemia cell line HL-60 (ATCC, CCL-240) were cultured in RPMI-1640 supplemented with 20% hiFBS (ThermoFisher, 10-438-026). Cultures were thoroughly washed with prewarmed complete media when bringing out of cryostorage to completely remove DMSO, as residual DMSO can induce differentiation in HL-60s.[66] Cells were allowed to recover for at least two weeks prior to any NETosis experiments. Cultures were not allowed to exceed a density of 5e5 cells per mL of culture media, as high densities can also induce differentiation.[66]

To induce differentiation of HL-60's, 2e6 cells were harvested by centrifugation (300 rcf, 5 min) and resuspended in complete media (RPMI-1640 +20% hiFBS) supplemented with 100 nM ATRA (Sigma-Aldrich, R2625) and DMSO (Sigma-Aldrich, D8414). Cells were cultured for 5-6 days before use, with a complete media change 48 h prior to use.

NETosis assays.

For live cell NETosis assays were performed in 96 well plates (Corning, 3595) and monitored by fluorescence microscopy with an Incucyte S3 (Essen Biosciences) or an Incucyte ZOOM (Essen Biosciences). DNA staining was performed using membrane impermeable fluorogenic DNA intercalators Cytotox Green (Essen Biosciences, 4633) or Cytotox Red (Essen Biosciences, 4632).

Plates were prepared containing 10X solutions of compounds (20 µL) and a 2X solution of DNA dye (100 µL) in serum-free media (IMDM for primary neutrophils, RPMI-1640 for HL-60s) lacking phenol red. Freshly harvested neutrophils in media (IMDM with 1.2% hiFBS for primary neutrophils for 0.5% final concentration of hiFBS, serum free RPMI-1640 for HL-60s) were then added to the plate (80 µL, 2.5e5 per mL, 2e4 per well) from a cell suspension. The plates were briefly centrifuged at 300 rcf for 1 min to settle the cell suspension, and the plates were immediately transferred to the Incucyte for periodic monitoring (every 10 min for 8 h or every 15 min for 12 h).

For NETosis assays with diluted COVID-19 plasma, freshly isolate neutrophils were plated on 96 well plates (Corning, 3595) coated with 0.01% poly-L-lysine (Sigma, P4707) in IMDM supplemented with 0.5% hiFBS. The neutrophils were allowed to settle and adhere for 20 min before the media was removed and IMDM containing 10% healthy or COVID-19 plasma and with or without glycopolypeptide (500 nM) was added. Alternatively, control wells were treated with no inducer, PMA (500 nM) or R848 (10 µM) in IMDM with 0.5% hiFBS. Plates were incubated for 4 h at 37 °C and the media was gently removed. The cells were then fixed for 15 min at room temperature in a solution of 4% PFA in PBS (ThermoFisher, FB002). The fixed

cells were then blocked in 10% goat serum in PBS, stained with anti-H1/DNA (EMD Millipore, MAB3864), and visualized with anti-mouse AlexaFluor 594 (Jackson ImmunoResearch, 115-585-174). Plates were imaged using an Incucyte S3.

For NETosis assays with undiluted COVID-19 plasma, freshly isolate neutrophils were plated on black-walled half-area 96 well plates (Greiner, 675090) coated with 0.01% poly-L-lysine (Sigma, P4707) in IMDM supplemented with 0.5% hiFBS. The neutrophils were allowed to settle and adhere for 20 min before the media was removed and either healthy or COVID-19 plasma and with or without glycopolypeptide (500 nM) was added. Alternatively, control wells were treated with no inducer or R848 (10 µM) in IMDM with 0.5% hiFBS. Plates were incubated for 4 h at 37 °C and the media was gently removed. The cells were then fixed for 15 min at room temperature in a solution of 4% PFA in PBS (ThermoFisher, FB002). The fixed cells were washed. Then cells were then blocked in 10% goat serum. For plates imaged by Incucyte S3, cells were stained with anti-H1/DNA (EMD Millipore, MAB3864) and visualized with a combination of anti-mouse AlexaFluor 594 (Jackson ImmunoResearch, 115-585-174) and MemGlow488 (Cytoskeleton, MG01-02). For plates imaged by immunofluorescence using a Keyence BZ-710, cells were stained with anti-MPO (Thermo Scientific, MA516383) and visualized with anti-rabbit AlexaFluor 555 (Thermo Scientific, A27039). Cells were imaged in HBSS containing DAPI imaging solution (Thermo Scientific, R37606). Images were collected using a Keyence BZ-X710 and images were analyzed using ImageJ.

Incucyte images were analyzed using the onboard Incucyte analysis software. For Incucyte S3 analyses: phase images were analyzed to identify cells using the following settings: segmentation adjustment = 0.8; minimum area filter = 25 μm^2. For primary neutrophils,

fluorescence areas were determined using the following settings: top hat segmentation; radius (µm) = 10.0; threshold = 10.0 GCU or 0.1 RCU; area filter = 300 µm^2. For dHL-60s, fluorescence areas were determined as for primary neutrophils with the following variation: area filter = 200 µm^2. For Incucyte ZOOM analyses: phase images were analyzed to identify cells using the following settings: segmentation adjustment = 0.8; minimum area filter = 25 µm^2. For primary neutrophils, fluorescence areas were determined using the following settings: top hat segmentation; radius (µm) = 10.0; threshold = 5.0 GCU; area filter = 200 µm^2

Reactive oxygen species measurements.

Induction of reactive oxygen species was measured by fluorescence microscopy using an Incucyte S3 (Essen Biosciences). Cells were prepared as for NETosis assays, with the difference that rather than the inclusion of Cytotox dye in the media, CellROX Deep Red (Thermo Fisher, C10422) was included at a final concentration of 5 µM. Data were analyzed as in NETosis assays, with the following changes in settings for quantifying red fluorescence: top hat segmentation; radius (µm) = 10.0; threshold = 1.6 RCU; area filter = 25 µm^2.

siRNA knock downs.

For siRNA knock down experiments, HL-60's were differentiated as indicated above. On day 4, the media was changed and 3 mL of culture was transfected with 30 pmol siRNA's (IDT) using Lipofectamine RNAiMAX (Thermo Fisher, 13778100) according to the manufacturer's instructions. Transfectants were cultured for 48 h prior to use in NETosis assays, with a complete media change at 24 h post transfection. Protein expression was validated by Western blot or flow cytometry, as applicable.

For siRNA KD of SIGLEC9, the top two suggested predesigned dicer substrate siRNA's from IDT (hs.Ri.SIGLEC9.13.1 and hs.Ri.SIGLEC9.13.2) were combined in a 1:1 molar ratio. For siRNA KD of PTPN6, the top suggested predesigned dicer substrate siRNA (hs.Ri.PTPN6.13.1) was used. As a negative control, scramble siRNA's were obtained from IDT.

Flow cytometry.

All flow cytometry experiments were performed using a BD Accuri 6 flow cytometer and analyzed using FlowJo 10. For all flow cytometry experiments, live cells were isolated from culture and resuspended in cold PBS supplemented with 1% BSA at a concentration of 1e7 cells per mL. Aliquots of 5e5 cells were then stained at the concentrations indicated in the Reagents Table and Usage for 30 min on ice in the dark. Cells were then washed three times (500 rcf, 5 min) with in cold PBS supplemented with 1% BSA before being analyzed by flow cytometry.

SDS-PAGE and Western blotting.

Cell pellets were washed twice with cold PBS supplemented with 1 mM EDTA and were lysed in RIPA buffer (50 µL for each 1e6 cells) (Thermo Fisher, PI89900) supplemented with Benzonase (1:1000) (Sigma Aldrich, E1014), HALT phosphatase inhibitor (1:100) (Thermo Fisher, 78420), and HALT protease inhibitor (1:100) (Thermo Fisher, 87786) for 30 min at 4 °C. Lysates were clarified by centrifugation at 4 °C for 15 min at 16000 rcf. Protein concentration was quantified by Rapid Gold BCA (Thermo Fisher, A53226).

Lysates were diluted into SDS-buffer with beta-mercaptoethanol and were separated by SDS-PAGE on 4-12% bisacrylamide gels loading 10 µg per lane. For analysis of histone H3 citrullination, lysates were separated in XT-MES at 200 V for 35 min. For analysis of SHP-1 levels after siRNA KD, lysates were separated in XT-MOPS at 200 V for 1 h. Blots were transferred to nitrocellulose and blocked with 5% BSA in TBS before being stained with primary antibodies and IR-dye conjugated secondary antibodies for analysis by LiCOR.

Protein expression and purification.

All proteins for enzymatic synthesis of glycopolypeptides were expressed and purified as previously described.[41]

His-tagged proteins cultures were grown at 37 °C to an OD600 of 0.8-1.0 in 1 L of LB containing the appropriate antibiotic selection marker, at which point expression was induced with IPTG (0.1 mM) and cultures were grown overnight at 20 °C with shaking at 220 rpm. After 24h, cells were pelleted by centrifugation and lysed in buffer (250 mM TrisHCl, 0.5 M NaCl, 20 mM imidazole, 0.1% TritonX100) supplemented with protease inhibitor cocktail (Sigma Aldrich, 04693132001) (one tablet per 40 mL) and DNAseI (Thermo Fisher, 90083) (10 µL per 40 mL). Cells were lysed using a dounce homogenizer followed by French press. Lysates were clarified by centrifugation and purified on HisTRAP columns (GE Life Sciences, 17-5247-01) using a gradient of 20 mM to 200 mM imidazole on an AKTA FPLC. Fraction purity was determined by SDS-PAGE and pure fractions were combined, purified by dialysis against storage buffer (50 mM Tris HCl, 250 mM NaCl, 10% glycerol), aliquoted, and flash-frozen in liquid nitrogen for storage in a -80 °C freezer.

Phosphoproteomics.

Primary neutrophils were treated in media containing the indicated compounds in IMDM [+] 0.5% hiFBS for the indicated time period, or in plasma from either healthy donors or COVID-19 patients, with or without pS9L (500 nM) for 15 min. Cell pellets were washed twice with cold PBS supplemented with 1 mM EDTA and were lysed in RIPA buffer (50 uL for each 1e6 cells) (Thermo Fisher, PI89900) supplemented with Benzonase (1:1000) (Sigma Aldrich, E1014), HALT phosphatase inhibitor (1:100) (Thermo Fisher, 78420), and HALT protease inhibitor (1:100) (Thermo Fisher, 87786) for 30 min at 4 °C. Lysates were clarified by centrifugation at 4 °C for 15 min at 16000 rcf. Protein concentration was quantified by Rapid Gold BCA (Thermo Fisher, A53226).

Digestion was performed on 100 µg protein using a mini S-trap protocol provided by the manufacturer (Protifi).[67] Here, proteins brought to 5% SDS and reduced with 5 mM DTT for 10 minutes at 95 C. Cysteines were alkylated using 30 mM iodoacetamide for 45 minutes each at room temperature in the dark. The lysate was then acidified with phosphoric acid, brought to approximately 80-90% methanol with 100 mM TEAB in 90% methanol, and loaded onto the S-trap column. Following washing with 100 mM TEAB in 90% methanol, trypsin (Promega) was added to the S-trap at a 20:1 protein:protease ratio for 90 minutes at 47 °C. Peptides from each lysate were labeled with 11-plex TMT (Tandem Mass Tags, Thermo Fisher Scientific) for 2 hours at room temperature using recently published protocols.[47,68] Labeling schemes for the stimulated study comparing R848 and PMA to no treatment (NT) were: NT replicates in channels 126C (Donor 1), 127N (Donor 2), and 130C (Donor 3); PMA replicates in 127C (Donor 1), 128N (Donor 2) and 131N (Donor 3); R848 replicates in 128C (Donor 1), 129N (Donor 2) and 131C (Donor 3). For the polymer experiment, the labeling scheme was: vehicle replicates in channels 126C (Donor 1), 127N (Donor 2), and 130C (Donor 3); pS9L replicates in 127C (Donor 1), 128N (Donor 2) and 131N (Donor 3); pLac replicates in 128C (Donor 1), 129N (Donor 2) and 131C (Donor 3). A test mix was run to confirm >99% labeling efficiency and even distribution of

signal across all channels prior to quenching of the TMT labeling reaction (0.5 uL 50% hydroxylamine reacted for 15 min). Peptides from each channel were then combined prior to phosphopeptide enrichment, which was performed as previously described.[69] Briefly, 100 µL magnetic titanium(IV) immobilized metal ion affinity chromatography (Ti(IV)-IMAC, ReSyn Biosciences) beads were washed three times with 1 mL 80% acetonitrile/6% TFA (all washes were 1 mL).[70] Peptides were dissolved in 1 mL 80% acetonitrile/6% TFA and gently vortexed with the TI(IV)-IMAC beads for 45 minutes. Unbound peptides were kept as flow through for total protein analysis, followed by three 80% acetonitrile/6% TFA, one 80% acetonitrile, one 0.5 M glycolic acid/80% acetonitrile, and two 80% acetonitrile washes. Peptides were eluted with 500 µL 50% acetonitrile, 1% ammonium hydroxide. Both eluate and flow through were dried down in a speed vac and further cleaned up on Strata-X SPE cartridges (Phenomenex) by conditioning the cartridge with 1 mL ACN followed by 1 mL 0.2% formic acid (FA) in water. Peptides were resuspended in 0.2% FA in water and then loaded on to the cartridge, followed by a 1 mL wash with 0.2% FA in water. Peptides were eluted with 400 uL of 0.2% FA in 80% ACN, were dried via lyophilization.

All samples were resuspended in 0.2% formic acid in water prior to LC-MS/MS analysis. Total protein samples were resuspended in 500 µL with 1 µL injected on column, while enriched phosphopeptides were resuspended in 15 µL total with 4 µL injected per analysis. Triplicate injections were collected for all samples. All (phospho)peptide mixtures were separated over a 25 cm EasySpray reversed phase LC column (75 µm inner diameter packed with 2 µm, 100 Å, PepMap C18 particles, Thermo Fisher Scientific). The mobile phases (A: water with 0.2% formic acid and B: acetonitrile with 0.2% formic acid) were driven and controlled by a Dionex Ultimate 3000 RPLC nano system (Thermo Fisher Scientific). An integrated loading pump was used to load peptides onto a trap column (Acclaim PepMap 100 C18, 5 um particles, 20 mm length,

Thermo Fisher Scientific) at 8 µL/min, which was put in line with the analytical column 4 minutes into the gradient for the total protein samples. The gradient increased from 0% to 5% B over the first 4 minutes of the analysis, followed by an increase from 5% to 25% B from 4 to 158 minutes, an increase from 25% to 90% B from 158 to 162 minutes, isocratic flow at 90% B from 162 to 168 minutes, and a re-equilibration at 0% for 12 minutes for a total analysis time of 180 minutes. Eluted (phoshpo)peptides were analyzed on an Orbitrap Fusion Tribrid MS system (Thermo Fisher Scientific). Precursors were ionized using an EASY-Spray ionization source (Thermo Fisher Scientific) source held at +2.2 kV compared to ground, and the column was held at 40 °C. The inlet capillary temperature was held at 275 °C. Survey scans of peptide precursors were collected in the Orbitrap from 350-1350 Th with an AGC target of 1,000,000, a maximum injection time of 50 ms, and a resolution of 60,000 at 200 m/z. Monoisotopic precursor selection was enabled for peptide isotopic distributions, precursors of z = 2-5 were selected for data-dependent MS/MS scans for 2 second of cycle time, and dynamic exclusion was set to 30 seconds with a ±10 ppm window set around the precursor monoisotope. An isolation window of 1 Th was used to select precursor ions with the quadrupole. MS/MS scans were collected using HCD at 30 normalized collision energy (nce) with an AGC target of 100,000 and a maximum injection time of 118 ms. Mass analysis was performed in the Orbitrap with a resolution of 60,000 with a first mass set at 100 Th.

Phosphoproteomic data analysis.

All data were searched with the Andromeda search engine[71] in MaxQuant[72] using the entire human proteome downloaded from Uniprot[73] (reviewed, 20428 entries). Each separate TMT experiment (resting, activated, and pLac control) was searched separately, with the flow through/total protein triplicate injections labeled as Group0 and False under “PTM” and phosphopeptide enriched triplicate injections labeled as Group1 and True under “PTM”. Group0

had cleavage specificity set to Trypsin/P with 2 missed cleavage allowed and variable modifications of oxidation of methionine and acetylation of the protein N-terminus with 4 maximum modifications per peptide. Group1 had cleavage specificity set to Trypsin/P with 3 missed cleavage allowed and variable modifications of phosphorylation on serine/threonine/tyrosine, oxidation of methionine, and acetylation of the protein N-terminus with 4 maximum modifications per peptide. The experiment type for both Group0 and Group1 was set to Reporter ion MS2 and only TMT channels used (as described above) were selected to be included. The reporter ion mass tolerance was set to 0.3 Da and the minimum reporter PIF score was set to 0.75. Defaults were used for the remaining settings, including PSM and protein FDR thresholds of 0.01 and 20 ppm, 4.5 ppm, and 20 ppm for first search MS1 tolerance, main search MS1 tolerance, and MS2 product ion tolerance, respectively. Match between runs was not enabled. Quantified phosphosites were then processed in Perseus.[74] Contaminants and reverse hits were removed, results were filtered for phosphosites that had localization probabilities > 0.75, and signal in all relevant TMT channels was required. Significance testing was performed using a two-tailed pair-ed sample t-test calculated in Microsoft Excel, using one condition versus control (NT or vehicle for stimulated and polymer experiments, respectively) for pairwise comparisons. Data have been deposited to the ProteomeXchange Consortium via the PRIDE partner repository with the dataset identifier PXD022990.[75]

Analysis of publicly-available single-cell RNA-sequencing (scRNA-seq) data.

The open source statistical software R (www.r-project.org; v3.6.1) and the R package Seurat (v 3.2.2) was used for scRNA-seq data analysis.[76] A pre-processed Seurat object containing scRNA-seq data and metadata of neutrophils profiled using the BD Rhapsody platform was retrieved from www.fastgenomics.org as outlined in the data availability statement of Schulte-Schrepping, et al.[8] The average expression of *SIGLEC9* or *PADI4* was defined as the mean of

log-normalized transcript counts, calculated by NormalizeData() function, in a given sample. DotPlot() was used to visualize average and percent expression of *SIGLEC9* or *PADI4*.

Reagent Table and Usage.

IN – Incucyte S3 (microscopy); OC – Octet (*in vitro* protein binding); FC – flow cytometry; WB – western blot; KD – siRNA knock down; IF – immunofluorescence

Reagent	**Source (#)**	**Usage, dilution/concentration**
Cytotox Green	Essen Biosciences (4633)	IN, 1:4,000
Cytotox Red	Essen Biosciences (4632)	IN, 1:4,000
CellROX Deep Red	ThermoFisher (C10422)	IN, 1:500
Anti-Siglec-9 clone K8 / AlexaFluor 647	BioLegend (351509)	FC, 1:50
Anti-human CD45 clone HI30 / APC	Stemcell Tecnologies (60018AZ.1)	FC, 1:50
Anti-human CD16 clone 3G8 / AlexaFluor 488	Stemcell Technologies (60041AD.1)	FC, 1:50
Mouse IgG1 isotype clone MOPC-21 / FITC	BD Biosciences (551954)	FC, 1:50
Mouse IgG1 isotype clone MOPC-21 / APC	BD Biosciences (550854)	FC, 1:50
Siglec-9-Fc	R&D Systems (1139-SL-050)	OC, 400 nM
DsiRNA (SIGLEC9)	IDT (hs.Ri.SIGLEC9.13.1)	KD, 30 nM
DsiRNA (SIGLEC9)	IDT (hs.Ri.SIGLEC9.13.2)	KD, 30 nM
DsiRNA (PTPN6)	IDT (hs.Ri.PTPN6.13.1)	KD, 30 nM
siRNA negative control	IDT (51-01-19-08)	KD, 30 nM
Rabbit anti-CitH3 (R2/R8/R17)	Abcam (ab5103)	WB, 1:1,000
Mouse anti-GAPDH	Sigma-Aldrich (G8795-100UL)	WB, 1:10,000
NSC-87877	Sigma-Aldrich (565851-50MG)	IN, 50 µM

Rabbit anti-SHP1 (clone Y476)	Abcam (ab32559)	WB, 1:1,000
goat anti-mouse 680RD	LiCOR (926-68070)	WB, 1:10,000
goat anti-rabbit 800CW	LiCOR (926-32211)	WB, 1:10,000
anti-H1/DNA	EMD Millipore (MAB3864)	IF, 1:100
goat anti-mouse AlexaFluor 594	Jackson ImmunoResearch (115-585-174)	IF, 1:1000
MemGlow488	Cytoskeleton (MG01-02)	IF, 1:200
anti-myeloperoxidase clone SP72	Thermo Scientific (MA516383)	IF, 1:100
goat anti-rabbit AlexaFluor 555	Thermo Scientific (A27039)	IF, 1:1000
DAPI solution	Thermo Scientific (R37606)	IF, 2 drops per mL

1018

1019